Quantifying prior probabilities for disease-causing variants reveals the top genetic contributors in inborn errors of immunity

Quant Group[1], Simon Boutry[2], Ali Saadat[2], Maarja Soomann[3], Johannes Trück[3], D. Sean Froese[4], Jacques Fellay[2], Sinisa Savic[5], Luregn J. Schlapbach[6], and Dylan Lawless *[6]

[1]The quantitative omic epidemiology group.
[2]Global Health Institute, School of Life Sciences, École Polytechnique Fédérale de Lausanne, Switzerland.
[3]Division of Immunology and the Children's Research Center, University Children's Hospital Zurich, University of Zurich, Zurich, Switzerland.
[4]Division of Metabolism and Children's Research Center, University Children's Hospital Zürich, University of Zurich, Zurich, Switzerland.
[5]Leeds Institute of Rheumatic and Musculoskeletal Medicine, University of Leeds, Leeds, UK.
[6]Department of Intensive Care and Neonatology, University Children's Hospital Zurich, University of Zurich, Zurich, Switzerland.

July 1, 2025

Abstract

Background: Accurate interpretation of genetic variants requires quantifying the probability that a variant is disease-causing, including the possibility of unobserved causal alleles.

Methods: We developed a statistical framework that computes genome-wide prior probabilities for variant pathogenicity, integrating population allele frequencies, variant classifications, and Hardy-Weinberg expectations across inheritance modes. Bayesian modelling then combines these priors with patient data to produce credible intervals reflecting diagnostic confidence.

Results: We applied the framework to 557 genes implicated in inborn errors of immunity (IEI), generating variant-level probabilities now publicly accessible. Integrating these data with protein-protein interaction networks and immunophenotypic features revealed patterns of genetic constraint and refined disease classification. Validation in national cohorts demonstrated close agreement between predicted and observed case numbers.

Conclusions: Our method addresses a long-standing gap in clinical genomics by quantifying both observed and unobserved genetic evidence in disease diagnosis. Although demonstrated in IEI, it is broadly applicable and provides a quantitative basis for variant interpretation, clinical decision-making, and future genomic analyses. [1]

[1] * Addresses for correspondence: Dylan.Lawless@kispi.uzh.ch.

Availability: This data is integrated in public panels at https://iei-genetics.github.io. The source code are accessible as part of the variant risk estimation project at https://github.com/DylanLawless/var_risk_est and IEI-genetics project at https://github.com/iei-genetics/iei-genetics.github.io. The data is available from the Zenodo repository: https://doi.org/10.5281/zenodo.15111583 (VarRiskEst PanelAppRex ID 398 gene variants.tsv). VarRiskEst is available under the MIT licence.

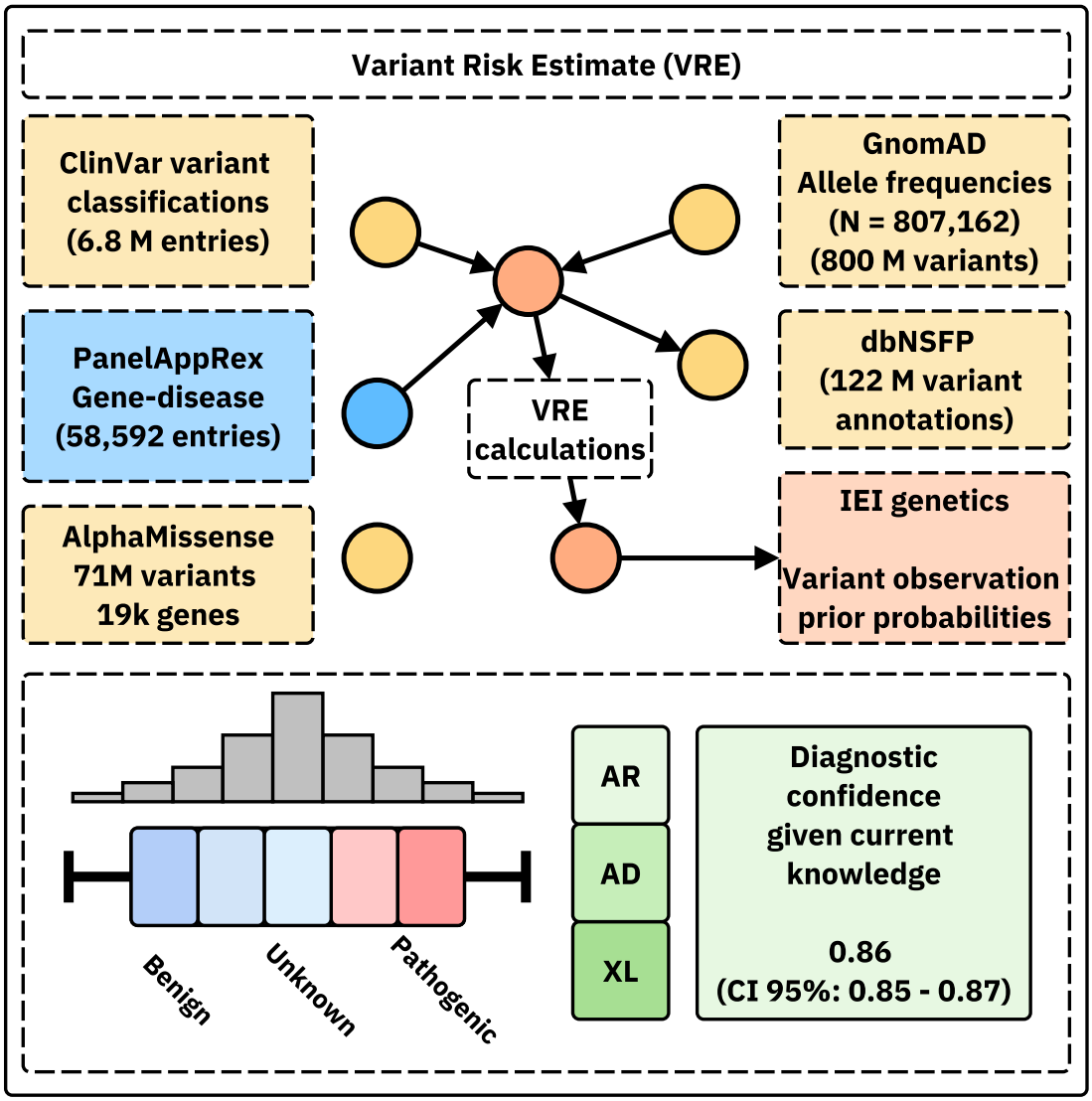

Graphical abstract.

Acronyms

1 Introduction

Accurately determining the probability that a patient harbours a disease-causing genetic variant remains a foundational challenge in clinical and statistical genetics. For over a century, the primary focus has been on identifying true positive (TP)s, pathogenic causal variants observed in affected individuals. Peer review and classification frameworks also work to suppress false positive (FP)s. However, two critical components of the genetic landscape have received far less attention: false negative (FN)s, where pathogenic variants are missed due to technical or interpretive limitations, and true negative (TN)s, which represent the vast majority of benign or non-causal variants. TNs are more commonly used in contexts such as cancer screening, where a negative result can provide reassurance that a panel of known actionable variants has been checked. Yet outside these specific uses, their broader statistical and clinical value is rarely leveraged. From a statistical perspective, FNs and TNs are an untapped goldmine. They hold essential information about what is not observed, what should be expected under baseline assumptions, and how confident one can be in the absence of a pathogenic finding. Yet these dimensions are rarely quantified, leaving a bias in current variant interpretation frameworks towards known TPs and lacking principled priors for genome-wide disease probability estimation.

Quantifying the risk that a patient inherits a disease-causing variant is a fundamental challenge in genomics. Classical statistical approaches grounded in Hardy-Weinberg Equilibrium (HWE) (1; 2) have long been used to calculate genetic probabilities for Single Nucleotide Variant (SNV)s. However, applying these methods becomes more complex when accounting for different Mode of Inheritance (MOI), such as Autosomal Recessive (AR) versus Autosomal Dominant (AD) or X-Linked (XL) disorders. In AR conditions, for example, the occurrence probability must incorporate both the homozygous state and compound heterozygosity, whereas for AD and XL disorders, a single pathogenic allele is sufficient to cause disease. Advances in genetic research have revealed that MOI can be even more complex (3). Mechanisms such as dominant negative effects, haploinsufficiency, mosaicism, and digenic or epistatic interactions can further modulate disease risk and clinical presentation, underscoring the need for nuanced approaches in risk estimation. Karczewski et al. (4) made significant advances; however, the remaining challenge lies in applying the necessary statistical genomics data across all MOI for any gene-disease combination. Preliminary approaches have been reported for diseases such Wilson disease, mucopolysaccharidoses, primary ciliary dyskinesia, and treatable metabolic diseasse, (5; 6), as reviewed by Hannah et al. (7).

To our knowledge, all approaches to date have been limited to single MOI, specific to the given disease, or restricted to a small number of genes. We argue that an integrated approach is both necessary and highly powerful because the resulting probabilities can serve as informative priors in a Bayesian framework for variant and disease probability estimation; a perspective that is often overlooked in clinical and statistical genetics. Such a framework not only refines classical HWE-based risk estimates but also has the potential to enrich clinicians' understanding of what to expect

in a patient and to enhance the analytical models employed by bioinformaticians.

The resulting dataset from these necessary calculations also holds value for AI and reinforcement learning applications, providing an enriched version of the data underpinning frameworks such as AlphaFold (8) and AlphaMissense (9).

This gap is not only due to conceptual limitations, but to the historical absence of large, harmonised reference datasets. Only recently have resources become available to support rigorous genome-wide probability estimation. These include high-resolution population allele frequencies (e.g. gnomAD v4 (4)), curated variant classifications (e.g. ClinVar (10)), functional annotations (e.g. UniProt (11)), and pathogenicity prediction models (e.g. AlphaMissense (9)). We previously introduced PanelAppRex to aggregate gene panel data from multiple sources, including Genomics England (GE) PanelApp, ClinVar, and Universal Protein Resource (UniProt), thereby enabling advanced natural searches for clinical and research applications (10–13). This earlier work relied on expert-curated panels, such as those from the NHS National Genomic Test Directory and the 100,000 Genomes Project, converted into machine-readable formats for rapid variant discovery and interpretation. Together, these resources now make it possible to model the expected distribution of variant types, frequencies, and classifications across the genome.

By reframing variant interpretation as a problem of calibrated expectation rather than solely reactive confirmation, our framework empowers clinicians and researchers to anticipate both observed and unobserved pathogenic burdens. This scalable, genome-wide approach promises to streamline diagnostic workflows, reduce uncertainty in inconclusive cases, inform statistical models and genetic epidemiology studies, and accelerate the integration of genetic insights into patient care.

In this study, we focused on reporting the probability of disease observation through genome-wide assessments of gene-disease combinations. We then focused on known Inborn Errors of Immunity (IEI) genes, sometimes called the "Primary Immunodeficiency (PID) or Monogenic Inflammatory Bowel Disease genes" (12–14), to validate our approach and demonstrate its clinical relevance. This application to a well-established genotype-phenotype set, comprising over 500 gene-disease associations, underscores its utility. The most recent update on the classification of IEI from the International Union of Immunological Societies (IUIS) expert committee was reported by Poli et al. (14), with an accompanying diagnostic guide (15). Our central hypothesis was that by using highly curated annotation data including population Allele Frequency (AF)s, disease phenotypes, MOI patterns, and variant classifications and by applying rigorous calculations based on HWE, we could accurately estimate the expected probabilities of observing disease-associated variants. Among other benefits, this knowledge can be used to derive genetic diagnosis confidence by incorporating these new priors.

2 Methods

2.1 Dataset

Data from Genome Aggregation Database (gnomAD) v4 comprised 807,162 individuals, including 730,947 exomes and 76,215 genomes (4). This dataset provided 786,500,648 SNVs and 122,583,462 Insertion/Deletion (InDel)s, with variant type counts of 9,643,254 synonymous, 16,412,219 missense, 726,924 nonsense, 1,186,588 frameshift and 542,514 canonical splice site variants. ClinVar data were obtained from the variant summary dataset (as of: 16 March 2025) available from the NCBI FTP site, and included 6,845,091 entries, which were processed into 91,319 gene classification groups and a total of 38,983 gene classifications; for example, the gene *A1BG* contained four variants classified as likely benign and 102 total entries (10). For our analysis phase we also used database for Non-Synonymous Functional Predictions (dbNSFP) which consisted of a number of annotations for 121,832,908 SNVs (16). The PanelAppRex core model contained 58,592 entries consisting of 52 sets of annotations, including the gene name, disease-gene panel ID, diseases-related features, confidence measurements. (12) Protein-Protein Interaction (PPI) network data was provided by Search Tool for the Retrieval of Interacting Genes/Proteins (STRINGdb), consisting of 19,566 proteins and 505,968 interactions (17). The Human Genome Variation Society (HGVS) nomenclature is used with Variant Effect Predictor (VEP)-based codes for variant IDs. AlphaMissense includes pathogenicity prediction classifications for 71 million variants in 19 thousand human genes (9; 18). We used these scores to compared against the probability of observing the same given variants. **Box 2.1** list the definitions from the IUIS IEI for the major disease categories used throughout this study (14).

The following genes were used for disease cohort validations and examples. We used the two most commonly reported genes from the IEI panel Nuclear Factor Kappa B Subunit 1 (*NFKB1*) (19–22) and Cystic Fibrosis Transmembrane Conductance Regulator (*CFTR*) (23–25) to demonstrate applications in AD and AR disease genes, respectively. We used Severe Combined Immunodeficiency (SCID)-specific genes AR DNA Cross-Link Repair 1C (*DCLRE1C*), AR Recombination activating gene 1 (*RAG1*), XL Interleukin 2 Receptor Subunit Gamma (*IL2RG*) to demonstrate a IEI subset disease phenotype of SCID. We also used AD Tumor necrosis factor, alpha-induced protein 3 (*TNFAIP3*) for other examples comparable to *NFKB1* since it is also causes AD pro-inflammatory disease but has more known ClinVar classifications at higher AF then *NFKB1*.

Box 2.1 Definitions for IEI Major Disease Categories

Major Category	Description
1. CID	Immunodeficiencies affecting cellular and humoral immunity
2. CID+	Combined immunodeficiencies with associated or syndromic features
3. PAD	Predominantly Antibody Deficiencies
4. PIRD	Diseases of Immune Dysregulation
5. PD	Congenital defects of phagocyte number or function
6. IID	Defects in intrinsic and innate immunity
7. AID	Autoinflammatory Disorders
8. CD	Complement Deficiencies
9. BMF	Bone marrow failure

2.2 Variant classification occurrence probability

To quantify the likelihood that an individual harbours a variant with a given disease classification, we compute the variant-level occurrence probability (variant risk estimate (VRE)) for each variant. As a starting point, we considered the classical HWE for a biallelic locus:

$$p^2 + 2pq + q^2 = 1,$$

where p is the allele frequency, $q = 1 - p$, p^2 represents the homozygous dominant, $2pq$ the heterozygous, and q^2 the homozygous recessive genotype frequencies. For disease phenotypes, particularly under AR MOI, the risk is traditionally linked to the homozygous state (p^2); however, to account for compound heterozygosity across multiple variants, we allocated the overall gene-level risk proportionally among variants.

Our computational pipeline estimated the probability of observing a disease-associated genotype for each variant and aggregated these probabilities by gene and ClinVar classification. This approach included all variant classifications, not limited solely to those deemed "pathogenic", and explicitly conditioned the classification on the given phenotype, recognising that a variant could only be considered pathogenic relative to a defined clinical context. The core calculations proceeded as follows:

1. Allele frequency and total variant frequency. For each variant i in a gene, the allele frequency was denoted as p_i. For each gene (any genomic region or set), we defined the total variant frequency (summing across all reported variants in that gene) as:

$$P_{\text{tot}} = \sum_{i \in \text{gene}} p_i.$$

Note that, because each calculation is confined to one gene, no additional scaling was required for our primary analyses (P_{tot}). However, if this same unscaled summation is applied across regions or variant sets of differing size or dosage sensitivity, it can bias burden estimates. In such cases, normalisation by region length or incorporation of gene- or region-specific dosage constraints is recommended.

If any of the possible SNV had no observed allele ($p_i = 0$), we assigned a minimal risk:

$$p_i = \frac{1}{\max(AN) + 1}$$

where $\max(AN)$ was the maximum allele number observed for that gene. This adjustment ensured that a nonzero risk was incorporated even in the absence of observed variants in the reference database.

2. Occurrence probability based on MOI. The probability that an individual is affected by a variant depends on the MOI. For **AD** and **XL** variants, a single pathogenic allele suffices:

$$p_{\text{disease},i} = p_i.$$

For **AR** variants, disease manifests when two pathogenic alleles are present, either as homozygotes or as compound heterozygotes. We use:

$$p_{\text{disease},i} = p_i \; P_{\text{tot}}.$$

Under HWE, the overall gene-level probability of an AR genotype is

$$P_{\text{AR}} \;=\; P_{\text{tot}}^2 \;=\; \sum_i p_i^2 \;+\; 2 \sum_{i<j} p_i \, p_j,$$

where $P_{\text{tot}} = \sum_i p_i$. A naïve per-variant assignment

$$p_i^2 + 2\, p_i \, (P_{\text{tot}} - p_i)$$

would, when summed over all i, double-count the compound heterozygous terms. To partition P_{AR} among variants without double counting, we allocate risk in proportion to each variant's allele frequency:

$$p_{\text{disease},i} = \frac{p_i}{P_{\text{tot}}} \times P_{\text{tot}}^2 = p_i \, P_{\text{tot}}.$$

This ensures

$$\sum_i p_{\text{disease},i} = \sum_i p_i \, P_{\text{tot}} = P_{\text{tot}}^2,$$

recovering the correct AR risk while attributing each variant its fair share of homozygous and compound-heterozygous contributions.

More simply, for AD or XL conditions a single pathogenic allele suffices, so the classification risk (e.g. benign, pathogenic) equals its population frequency. For AR conditions two pathogenic alleles are required - either two copies of the same variant or one copy each of two different variants, so we divide the overall recessive risk among variants according to each variant's share of the total classification frequency in that gene.

3. Expected case numbers and case detection probability. Given a population with N births (e.g. as seen in our validation studies, $N = 69\,433\,632$), the expected number of cases attributable to variant i was calculated as:

$$E_i = N \cdot p_{\text{disease},i}.$$

The probability of detecting at least one affected individual for that variant was computed as:

$$P(\geq 1)_i = 1 - \left(1 - p_{\text{disease},i}\right)^N.$$

4. Aggregation by gene and ClinVar classification. For each gene and for each ClinVar classification (e.g. "Pathogenic", "Likely pathogenic", "Uncertain significance", etc.), we aggregated the results across all variants. The classification grouping can be substituted by any alternative score system. The total expected cases for a given group was:

$$E_{\text{group}} = \sum_{i \in \text{group}} E_i,$$

and the overall probability of observing at least one case within the group was calculated as:

$$P_{\text{group}} = 1 - \prod_{i \in \text{group}} (1 - p_{\text{disease},i}) \,.$$

5. Data processing and implementation. We implemented the calculations within a High-Performance Computing (HPC) pipeline and provided an example for a single dominant disease gene, *TNFAIP3*, in the source code to enhance reproducibility. Variant data were imported in chunks from the annotation database for all chromosomes (1-22, X, Y, M).

For each data chunk, the relevant fields were gene name, position, allele number, allele frequency, ClinVar classification, and HGVS annotations. Missing classifications (denoted by ".") were replaced with zeros and allele frequencies were converted to numeric values. Subsequently, the variant data were merged with gene panel data from PanelAppRex to obtain the disease-related MOI mode for each gene. For each gene, if no variant was observed for a given ClinVar classification (i.e. $p_i = 0$), a minimal risk was assigned as described above. Finally, we computed the occurrence probability, expected cases, and the probability of observing at least one case of disease using the equations presented.

The final results were aggregated by gene and ClinVar classification and used to generate summary statistics that reviewed the predicted disease observation probabilities. We define the *VRE* as the prior probability of observing a variant classified as the cause of disease

6. Score-positive-total. For use as a simple summary statistic on the resulting user-interface, we defined the *score-positive-total* as the total number of positively scored variant classifications within a given region (gene, locus, or variant set). Using the ClinVar classification assigned to a scale from−5 (benign) to +5 (pathogenic), we included only scores > 0, corresponding to some evidence of pathogenicity. The score-positive-total yields a non-normalised estimate of the prior probability that a phenotype is explained by known pathogenic variants.

7. Classification scoring system. Each ClinVar classification was assigned an integer score: pathogenic = +5, likely pathogenic = +4, pathogenic (low penetrance) = +3, likely pathogenic (low penetrance) = +2, conflicting pathogenicity = +2, likely risk allele/risk factor/association = +1, drug response/uncertain significance/no classification/affects/other/not provided/uncertain risk allele = 0, protective = –3, likely benign = –4, benign = –5. No further normalisation was applied. The resulting distribution (**Figure S1 A-B**) is naturally comparable to a zero-centred average rank (**C-D**). This straightforward, modular approach can be readily replaced by any comparable evidence-based classification system. Variants with scores ≤ 0 were omitted,

since benign classifications do not inform disease likelihood in the score-positive-total summary.

2.3 Integrating observed true positives and unobserved false negatives into a single, actionable conclusion

In this section, we detail our approach to integrating sequencing data with prior classification evidence (e.g. pathogenic on ClinVar) to calculate the posterior probability of a complete successful genetic diagnosis. Our method is designed to account for possible outcomes of TP, TN, and FN, by first ensuring that all nucleotides corresponding to known variant classifications (benign, pathogenic, etc.) have been accurately sequenced. This implies the use of genomic variant call format (gVCF)-style data which refer to variant call format (VCF)s that contain a record for every position in the genome (or interval of interest) regardless of whether a variant was detected at that site or not. Only after confirming that these positions match the reference alleles (or novel unaccounted variants are classified) do we calculate the probability that additional, alternative pathogenic variants (those not observed in the sequencing data) could be present. Our Credible Interval (CrI) for pathogenicity thus incorporates uncertainty from the entire process, including the tally of TP, TN, and FN outcomes. We ignore the contribution of FPs as a separate task to be tackled in the future.

We estimated, for every query (e.g. gene or disease-panel), the posterior probability that at least one constituent allele is both damaging and causal in the proband. The workflow comprises four consecutive stages.

(i) Data pre-processing. We synthesized an example patient in a disease cohort of 200 cases. We made several scenarios where a causal genetic diagnosis based on the available data is either simple, difficult, or impossible. Our example focused on a proband two representative genes for AD IEI: *NFKB1* and *TNFAIP3*. All coding and canonical splice-region variants for *NFKB1* were extracted from the gVCF. We assumed a typical Quality Control (QC) scenario, where sites corresponding to previously reported pathogenic alleles were checked for read depth ≥ 10 and genotype quality ≥ 20. Positions that failed this check were labelled *missing*, thus separating true reference calls from non-sequenced or uninformative sequence.

(ii) Evidence mapping and occurrence probability. PanelAppRex variants were annotated with ClinVar clinical significance. Each label was converted to an ordinal evidence score $S_i \in [-5, 5]$ and rescaled to a pathogenic weight $W_i = \text{rescale}(S_i;\, -5, 5 \to 0, 1)$. This scoring system can be replaced with any comparable alternative. The HWE-based pipeline of Section 2.2 supplied a per-variant occurrence probability p_i. The adjusted prior was

$$p_i^* = W_i\, p_i, \qquad \text{and} \qquad \text{flag}_i \in \{\text{present}, \text{missing}\}.$$

(iii) Prior specification. In a hypothetical cohort of $n = 200$ diploid individuals the count of allele i follows a Beta-Binomial model. Marginalising the Binomial yields the Beta prior

$$\pi_i \sim \mathrm{Beta}\big(\alpha_i, \beta_i\big), \qquad \alpha_i = \mathrm{round}(2np_i^*) + \tilde{w}_i,\ \beta_i = 2n - \mathrm{round}(2np_i^*) + 1,$$

where $\tilde{w}_i = \max(1, S_i + 1)$ contributes an additional pseudo-count whenever $S_i > 0$.

(iv) Posterior simulation and aggregation. For each variant i we drew $M = 10\,000$ realisations $\pi_i^{(m)}$ and normalised within each iteration,

$$\tilde{\pi}_i^{(m)} = \frac{\pi_i^{(m)}}{\sum_j \pi_j^{(m)}}.$$

Variants with $S_i > 4$ were deemed to have evidence as *causal* (pathogenic or likely pathogenic). We note that an alternative evidence score or conditional threshold can be substituted for this step. Their mean posterior share $\bar{\pi}_i = M^{-1} \sum_m \tilde{\pi}_i^{(m)}$ and 95% CrI were retained. The probability that a damaging causal allele is physically present was obtained by a second layer:

$$P^{(m)} = \sum_{i:\, S_i > 3} \tilde{\pi}_i^{(m)}\, G_i^{(m)}, \qquad G_i^{(m)} \sim \mathrm{Bernoulli}(g_i),$$

with $g_i = 1$ for present variants, $g_i = 0$ for reference calls, and $g_i = p_i$ for missing variants. The gene-level estimate is the median of $\{P^{(m)}\}_{m=1}^{M}$ and its $2.5^{\text{th}}/97.5^{\text{th}}$ percentiles.

(v) Scenario analysis. The three scenarios were explored for a causal genetic diagnosis that is either simple, difficult, or impossible given the existing data. The proband spiked data had either: (1) known classified variants only, including only one known TP pathogenic variant, *NFKB1* `p.Ser237Ter`, (2) inclusion of an additional plausible yet non-sequenced splice-donor allele *NFKB1* `c.159+1G>A` (likely pathogenic) as a FN, and (3) where no known causal variants were present for a patient, one representative variant from each distinct ClinVar classification was selected and marked as unsequenced to emulate a range of putative FNs. The selected variants were: *TNFAIP3* `p.Cys243Arg` (pathogenic), `p.Tyr246Ter` (likely pathogenic), `p.His646Pro` (conflicting interpretations of pathogenicity), `p.Thr635Ile` (uncertain significance), `p.Arg162Trp` (not provided), `p.Arg280Trp` (likely benign), `p.Ile207Leu` (benign/likely benign), and `p.Lys304Glu` (benign). All subsequent steps were identical.

2.4 Validation of autosomal dominant estimates using *NFKB1*

To validate our genome-wide probability estimates in an AD gene, we focused on *NFKB1*. Our goal was to compare the expected number of *NFKB1*-related Common Variable Immunodeficiency (CVID) cases, as predicted by our framework, with the reported case count in a well-characterised national-scale PID cohort.

1. Reference dataset. We used a reference dataset reported by Tuijnenburg et al. (19) to build a validation model in an AD disease gene. This study performed whole-genome sequencing of 846 predominantly sporadic, unrelated PID cases from the NIHR BioResource-Rare Diseases cohort. There were 390 CVID cases in the cohort. The study identified *NFKB1* as one of the genes most strongly associated with PID. Sixteen novel heterozygous variants including truncating, missense, and gene deletion variants, were found in *NFKB1* among the CVID cases.

2. Cohort prevalence calculation. Within the cohort, 16 out of 390 CVID cases were attributable to *NFKB1*. Thus, the observed cohort prevalence was

$$\text{Prevalence}_{\text{cohort}} = \frac{16}{390} \approx 0.041,$$

with a 95% confidence interval (using Wilson's method) of approximately (0.0254, 0.0656).

3. National estimate based on literature. Based on literature (19; 20; 22), the prevalence of CVID in the general population was estimated as

$$\text{Prevalence}_{\text{CVID}} = \frac{1}{25\,000}.$$

For a UK population of $N_{\text{UK}} \approx 69\,433\,632$, the expected total number of CVID cases was

$$E_{\text{CVID}} \approx \frac{69\,433\,632}{25\,000} \approx 2777.$$

Assuming that the proportion of CVID cases attributable to *NFKB1* is equivalent to the cohort estimate, the literature extrapolated estimate is Estimated NFKB1 cases $\approx 2777 \times 0.041 \approx 114$, with a median value of approximately 118 and a 95% confidence interval of 70 to 181 cases (derived from posterior sampling).

4. Bayesian adjustment. Recognising that the sequenced cohort cases likely captures the majority of *NFKB1*-related patients (apart from close relatives), but may still miss rare or geographically dispersed variants, we combined the cohort-based and literature-based estimates using two complementary Bayesian approaches:

1. **Weighted adjustment (emphasising the cohort, $w = 0.9$):** We assigned 90% weight to the directly observed cohort count (16) and 10% to the extrapolated population estimate (114), thereby accounting, illustratively, for a small fraction of unobserved cases while retaining confidence in our well-characterised cohort:

$$\text{Adjusted Estimate} = 0.9 \times 16 \; + \; 0.1 \times 114 \; \approx \; 26,$$

yielding a 95% CrI of roughly 21 to 33 cases.

2. **Mixture adjustment (equal weighting, $w = 0.5$):** To reflect greater uncertainty about how representative the cohort is, we combined cohort and population prevalences equally. We sampled from the posterior distribution of the cohort prevalence,

$$p \sim \text{Beta}(16 + 1,\, 390 - 16 + 1),$$

and mixed this with the literature-based rate at 50% each (19; 20; 22). This yields a median estimate of 67 cases and a wider 95% CrI of approximately 43 to 99 cases, capturing uncertainty in both under-ascertainment and over-generalisation.

5. Predicted total genotype counts. The predicted total synthetic genotype count (before adjustment) was 456, whereas the predicted total genotypes adjusted for `synth_flag` was 0. This higher synthetic count was set based on a minimal risk threshold, ensuring that at least one genotype is assumed to exist (e.g. accounting for a potential unknown de novo variant) even when no variant is observed in gnomAD (as per **section 2.2**).

6. Validation test. Thus, the expected number of *NFKB1*-related CVID cases derived from our genome-wide probability estimates was compared with the observed counts from the UK-based PID cohort. This comparison validates our framework for estimating disease incidence in AD disorders.

2.5 Validation study for autosomal recessive CF using *CFTR*

To validate our framework for AR diseases, we focused on Cystic Fibrosis (CF). For comparability sizes between the validation studies, we analysed the most common SNV in the *CFTR* gene, typically reported as `p.Arg117His` (GRCh38 Chr 7:117530975 G/A, MANE Select HGVSp ENST00000003084.11: p.Arg117His). Our goal was to validate our genome-wide probability estimates by comparing the expected number of CF cases attributable to the `p.Arg117His` variant in *CFTR* with the nationally reported case count in a well-characterised disease cohort (23–25).

1. Expected genotype counts. Let p denote the allele frequency of the `p.Arg117His` variant and q denote the combined frequency of all other pathogenic *CFTR* variants, such that

$$q = P_{\text{tot}} - p \quad \text{with} \quad P_{\text{tot}} = \sum_{i \in \text{CFTR}} p_i.$$

Under Hardy–Weinberg equilibrium for an AR trait, the expected frequencies were:

$$f_{\text{hom}} = p^2 \quad \text{(homozygous for p.Arg117His)}$$

and

$$f_{\text{comphet}} = 2p\,q \quad \text{(compound heterozygotes carrying p.Arg117His and another pathogenic allele).}$$

For a population of size N (here, $N \approx 69\,433\,632$), the expected number of cases were:

$$E_{\text{hom}} = N \cdot p^2, \quad E_{\text{comphet}} = N \cdot 2p\,q, \quad E_{\text{total}} = E_{\text{hom}} + E_{\text{comphet}}.$$

2. Mortality adjustment. Since CF patients experience increased mortality, we adjusted the expected genotype counts using an exponential survival model (23–25). With an annual mortality rate $\lambda \approx 0.004$ and a median age of 22 years, the survival factor was computed as:

$$S = \exp(-\lambda \cdot 22).$$

Thus, the mortality-adjusted expected genotype count became:

$$E_{\text{adj}} = E_{\text{total}} \times S.$$

3. Bayesian uncertainty simulation. To incorporate uncertainty in the allele frequency p, we modelled p as a beta-distributed random variable:

$$p \sim \text{Beta}(p \cdot \text{AN}_{\text{eff}} + 1,\ \text{AN}_{\text{eff}} - p \cdot \text{AN}_{\text{eff}} + 1),$$

using a large effective allele count (AN_{eff}) for illustration. By generating 10,000 posterior samples of p, we obtained a distribution of the literature-based adjusted expected counts, E_{adj}.

4. Bayesian Mixture Adjustment. Since the national registry may not capture all nuances (e.g., reduced penetrance) of *CFTR*-related disease, we further combined the literature-based estimate with the observed national count (714 cases from the UK Cystic Fibrosis Registry 2023 Annual Data Report) using a 50:50 weighting:

$$E_{\text{Bayes}} = 0.5 \times (\text{Observed Count}) + 0.5 \times E_{\text{adj}}.$$

5. Validation test. Thus, the expected number of *CFTR*-related CF cases derived from our genome-wide probability estimates was compared with the observed counts from the UK-based CF registry. This comparison validated our framework for estimating disease incidence in AD disorders.

2.6 Validation of SCID-specific estimates using PID–SCID genes

To validate our genome-wide probability estimates for diagnosing a genetic variant in a patient with an PID phenotype, we focused on a subset of genes implicated in SCID. Given that the overall panel corresponds to PID, but SCID represents a rarer subset, the probabilities were converted to values per million PID cases.

1. Incidence conversion. Based on literature, PID occurs in approximately 1 in 1,000 births, whereas SCID occurs in approximately 1 in 100,000 births. Consequently, in a population of 1,000,000 births there are about 1,000 PID cases and 10 SCID cases. To express SCID-related variant counts on a per-million PID scale, the observed SCID counts were multiplied by 100. For example, if a gene is expected to cause SCID in 10 cases within the total PID population, then on a per-million PID basis the count is $10 \times 100 = 1{,}000$ cases (across all relevant genes).

2. Prevalence calculation and data adjustment. For each SCID-associated gene (e.g. *IL2RG*, *RAG1*, *DCLRE1C*), the observed variant counts in the dataset were adjusted by multiplying by 100 so that the probabilities reflect the expected number of cases per 1,000,000 PID. In this manner, our estimates are directly comparable to known counts from SCID cohorts, rather than to national population counts as in previous validation studies.

3. Integration with prior probability estimates. The predicted genotype occurrence probabilities were derived from our framework across the PID gene panel. These probabilities were then converted to expected case counts per million PID cases by multiplying by 1,000,000. For instance, if the probability of observing a pathogenic variant in *IL2RG* is p, the expected SCID-related count becomes $p \times 10^6$. Similar conversions are applied for all relevant SCID genes.

4. Bayesian Uncertainty and Comparison with Observed Data. To address uncertainty in the SCID-specific estimates, a Bayesian uncertainty simulation was performed for each gene to generate a distribution of predicted case counts on a per-million PID scale. The resulting median estimates and 95% CrIs were then compared against known national SCID counts compiled from independent registries. This comparison permuted a direct evaluation of our framework's accuracy in predicting the occurrence of SCID-associated variants within a PID cohort.

5. Validation Test. Thus, by converting the overall probability estimates to a per-million PID scale, our framework was directly validated against observed counts for SCID.

2.7 Protein network and genetic constraint interpretation

A PPI network was constructed using protein interaction data from STRINGdb (17). We previously prepared and reported on this dataset consisting of 19,566 proteins and 505,968 interactions (https://github.com/DylanLawless/ProteoMCLustR). Node attributes were derived from log-transformed score-positive-total values, which informed both node size and colour. Top-scoring nodes (top 15 based on score) were labelled to highlight prominent interactions. To evaluate group differences in score-positive-total across major disease categories, one-way Analysis of Variance (ANOVA) was performed followed by Tukey Honestly Significant Difference (HSD) post hoc tests (and non-parametric Dunn's test for confirmation). GnomAD v4.1 constraint metrics data was used for the PPI analysis and was sourced from Karczewski et al. (4). This provided transcript-level metrics, such as observed/expected ratios, Loss-Of-function Observed/Expected Upper bound Fraction (LOEUF), Probability of being Loss-of-function Intolerant (pLI), and Z-scores, quantifying Loss-of-Function (LOF) and missense intolerance, along with confidence intervals and related annotations for 211,523 observations.

2.8 Gene set enrichment test

To test for overrepresentation of biological functions, the prioritised genes were compared against gene sets from MsigDB (including hallmark, positional, curated, motif, computational, GO, oncogenic, and immunologic signatures) and WikiPathways using hypergeometric tests with FUMA (26; 27). The background set consisted of 24,304 genes. Multiple testing correction was applied per data source using the Benjamini-Hochberg method, and gene sets with an adjusted P-value ≤ 0.05 and more than one overlapping gene are reported.

2.9 Deriving novel PID classifications by genetic PPI and clinical features

We recategorised 315 immunophenotypic features from the original IUIS IEI annotations, reducing the original multi-level descriptors (e.g. "decreased CD8, normal or decreased CD4") first to minimal labels (e.g."low") and second to binary outcomes (normal vs. not-normal) for T cells, B cells, neutrophils, and immunoglobulins Each gene was mapped to its PPI cluster derived from STRINGdb and Uniform Manifold Approximation and Projection (UMAP) embeddings from previous steps. We first tested for non-random associations between these four binary immunophenotypes and PPI clusters using χ^2 tests. To generate a data-driven PID classification, we trained a decision tree (rpart) to predict PPI cluster membership from the four immunophenotypic features plus the traditional IUIS Major and Subcategory labels. Hyperparameters (complexity parameter $= 0.001$, minimum split $= 10$, minimum bucket $= 5$, maximum depth $= 30$) were optimised via five-fold cross validation using the `caret` framework. Terminal node assignments were then relabelled according to each group's predominant abnormal feature profile.

2.10 Probability of observing AlphaMissense pathogenicity

We obtained the subset pathogenicity predictions from AlphaMissense via the AlphaFold database and whole genome data from the studies data repository(9; 18). The AlphaMissense data (genome-aligned and amino acid substitutions) were merged with the panel variants based on genomic coordinate and HGVSc annotation. Occurrence probabilities were log-transformed and adjusted (y-axis displaying log10(occurrence prob + 1e-5) + 5)), to visualise the distribution of pathogenicity scores across the residue sequence. A Kruskal-Wallis test was used to compare the observed disease probability across clinical classification groups.

2.11 Probability model definitions

Estimating disease risk requires accounting for both variant penetrance, $P(D \mid G)$, where D denotes the disease state and G the genotype, and the fraction of cases attributable to a given variant, $P(G \mid D)$. In a fully penetrant single-variant model ($P(D \mid G) = 1$), the lifetime risk $P(D)$ equals the genotype frequency $P(G)$. For an allele with population frequency p, this gives $P(D) = p^2$ for a recessive mode of inheritance and $P(D) = 2p(1-p) \approx 2p$ for a dominant mode. With incomplete penetrance, $P(D) = P(G)\,P(D \mid G)$, and when multiple variants contribute to disease,

$$P(D) = \frac{P(G)\,P(D \mid G)}{P(G \mid D)}.$$

Because both $P(D \mid G)$ and $P(G \mid D)$ are often uncertain, we integrate ClinVar clinical classifications, population allele frequencies and curated gene–disease associations, assuming James-Stein shrinkage to derive robust aggregate priors. By focusing on a filtered set of variants $\mathcal{V}$ where each $P(G_i \mid D)$ is the probability that disease D is attributable to variant i and assuming $\sum_{i \in \mathcal{V}} P(G_i \mid D) \approx 1$, we obtain calibrated estimates of genotype frequency $P(G)$ despite uncertainty in individual parameters.

3 Results

3.1 Occurrence probability across disease genes

Our study integrated large-scale annotation databases with gene panels from PanelAppRex to systematically assess disease genes by MOI (12). By combining population allele frequencies with ClinVar clinical classifications, we computed an expected occurrence probability for each SNV, representing the likelihood of encountering a variant of a specific pathogenicity for a given phenotype. We report these probabilities for 54,814 ClinVar variant classifications across 557 genes (linked dataset (28)).

We focused on panels related to Primary Immunodeficiency or Monogenic Inflammatory Bowel Disease, using PanelAppRex panel ID 398. **Figure 1** displays all reported ClinVar variant classifications for this panel. The resulting natural scaling system (-5 to +5) accounts for the frequently encountered combinations of classification labels (e.g. benign to pathogenic). The resulting dataset (28) is briefly shown in **Table 1** to illustrate that our method yielded estimates of the probability of observing a variant with a particular ClinVar classification.

Table 1: **Example of the first several rows from our main results for 557 genes of PanelAppRex's panel: (ID 398) Primary immunodeficiency or monogenic inflammatory bowel disease**. "ClinVar Significance" indicates the pathogenicity classification assigned by ClinVar, while "Occurrence Prob" represents our calculated probability of observing the corresponding variant class for a given phenotype. MOI shows the gene-disease-specific mode of inheritance. Additional columns, such as population allele frequency, are not shown. (28)

Gene	Panel ID	ClinVar Clinical Significance	GRCh38 Pos	HGVSc	HGVSp	MOI	Occurrence Prob
ABI3	398	Uncertain significance	49210771	c.47G>A	p.Arg16Gln	AR	0.000000007
ABI3	398	Uncertain significance	49216678	c.265C>T	p.Arg89Cys	AR	0.000000005
ABI3	398	Uncertain significance	49217742	c.289G>A	p.Val97Met	AR	0.000000002
ABI3	398	Uncertain significance	49217781	c.328G>A	p.Gly110Ser	AR	0.000000002
ABI3	398	Uncertain significance	49217844	c.391C>T	p.Pro131Ser	AR	0.000000015
ABI3	398	Uncertain significance	49220257	c.733C>G	p.Pro245Ala	AR	0.000000022
...	...	...	...	...	...	...	...

3.2 Integrating observed true positives and unobserved false negatives into a single, actionable conclusion

Having established a probabilistic framework for estimating the prior probability of observing disease-associated variants under different inheritance modes, we then applied this model to an example patient to demonstrate its potential for clinical genetics. The algorithm first verified that all known pathogenic positions have been sequenced and observed as reference (true negatives), and identified any positions that were either observed as variant (true positives) or not assessable due to missing

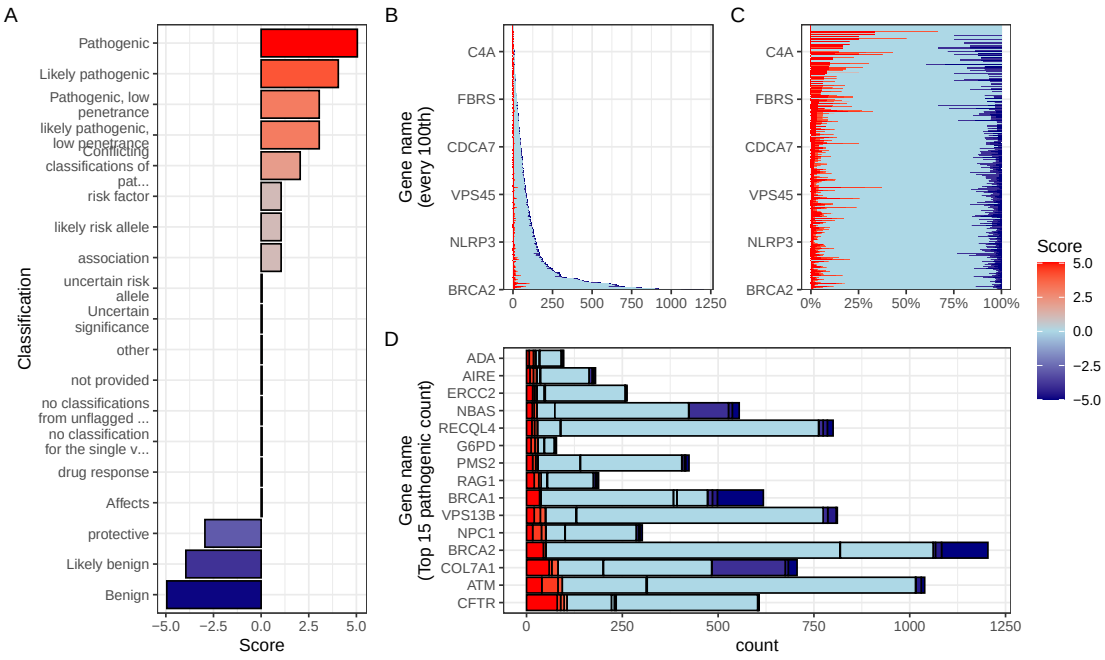

Figure 1: **Summary of ClinVar clinical significance classifications in the PID gene panel.** (A) Shows the numeric score coding for each classification (i.e. -5 benign to +5 pathogenic) as defined in methods Section 2.2. (B) Displays the stacked absolute count of classifications per gene. The same counts are shows as percentages per gene in (C). (D) For demonstration, the top 15 genes ranked by absolute count of pathogenic (score 5) variant classifications, indicating those most frequently occurring in the population as disease-causing.

sequence data of failed QC. These missing sites represent potential false negatives. By jointly modelling the observed and unobserved space, the method yielded a calibrated, evidence-weighted probability that at least one damaging causal variant could be present within a gene.

3.3 Scenario one - complete coverage and simple diagnosis

We present the results from three scenarios for an example single-case patient being investigated for the genetic diagnosis of IEI. **Figure S2** shows the results of the first simple scenario, in which only one known pathogenic variant, *NFKB1* `p.Ser237Ter`, was observed and all other previously reported pathogenic positions were successfully sequenced and confirmed as reference. In this setting, the model assigned the full posterior probability to the observed allele, yielding 100 % confidence that all present evidence supported a single, true positive causal explanation. The most strongly supported observed variant was `p.Ser237Ter` (posterior: 0.594). The strongest (probability of observing) non-sequenced variant was a benign variant `p.Thr567Ile` (posterior: 0). The total probability of a causal diagnosis given the available evidence was 1 (95%

CI: 1–1) (**Table S1**).

3.4 Scenario two - incomplete coverage and complex diagnosis

Figure 2 shows the second more complex scenario, where the same pathogenic variant *NFKB1* `p.Ser237Ter` was present, but coverage was incomplete at three additional sites of known classified variants. Among these was the likely-pathogenic splice-site variant *NFKB1* `c.159+1G>A`, which was not captured in the sequencing data. The panels of **Figure 2 (A–F)** illustrate the stepwise integration of observed and missing evidence, culminating in a posterior probability that reflects both confirmed findings and residual uncertainty. **Table 2** demonstrates our main goal and lists the final conclusion for reporting the clinical genetics results. **Table S2** lists the main metrics used to reach the conclusion (as illustrated in **Figure 2**).

Bayesian integration of every annotated allele yielded the quantitative CrIs for pathogenic attribution that (i) preserve Hardy-Weinberg expectations, (ii) accommodate AD, AR, XL inheritance, and (iii) carry explicit uncertainty for non-sequenced (or failed QC) genomic positions. The incremental calculation steps for the variant in question are shown in **Figure 2**.

First, **Figure 2 (A)** depicts the prior landscape where occurrence probabilities are partitioned by observed or missing status and by causal or non-causal evidence, with colour reflecting the underlying ClinVar score. **Figure 2 (B)** shows posterior normalisation which concentrates probability density on two high-confidence (high evidence score) alleles since the benign variants are, by definition, non-causal. **Figure 2 (C)** shows the resulting per-variant probability of being simultaneously damaging and causal; only the confirmed present (true positive) nonsense variant `p.Ser237Ter` and the (false negative) hypothetical splice-donor `c.159+1G>A` retain substantial support. Restricting the view to causal candidates in **Figure 2 (D)** confirms that posterior mass is distributed across these two variants. **Figure 2 (E)** decomposes the total damaging probability into observed (approximately 40 %) and missing (approximately 34 %) sources, whereas **Figure 2 (F)** summarises the gene-level posterior: inclusion of the splice-site allele (scenario 2) produces a median probability of 0.542 with a 95 % CrI of 0.264–0.8.

Numerically, the present variant `p.Ser237Ter` accounts for 0.399 of the posterior share, and the potentially causal but missing splice-donor allele `c.159+1G>A` contributes 0.339. The remaining alleles together explain a negligible share (**Table S2**). Thus, we can report that in this patient's scenario the probability of correct genetic diagnosis due to *NFKB1* `p.Ser237Ter` is 0.542 (95 % CrI of 0.264–0.8) given that a likely alternative remains to be confirmed for this patient. Upon confirmation that the second variant is not present, the confidence will rise to 1 (95 % CrI of 1–1) as shown in scenario one.

Table 2: Final variant report for clinical genetics scenario 2. Reported causal: `p.Ser237Ter` (posterior 0.377). Undetected causal: `c.159+1G>A` (posterior 0.364). The total probability of a causal diagnosis given the available evidence was 0.511 (95% CI: 0.237–0.774).

Parameter	present	missing
Gene	NFKB1	NFKB1
HGVSc	c.710C>G	c.159+1G>A
HGVSp	p.Ser237Ter	.
Inheritance	AD	AD
Patient sex	Male	Male
gnomAD frequency	6.57e-06	6.57e-06
95% CI lower	0.003	NA
p(median)	0.090	NA
95% CI upper	0.551	NA
Posterior p(causal)	0.377	0.364
Interpretation	Reported causal; variant observed	Reported causal; variant not detected — consider follow-up
Summary	Overall probability of correct causal diagnosis due to SNV/INDEL given the currently available evidence: 0.511 (95% CI 0.237–0.774).	

3.5 Scenario three - currently impossible diagnosis

Figure S3 shows the third scenario, in which no observed variants were detected in the proband for *NFKB1*. Instead, a broad range of plausible FN were detected as missing for the gene *TNFAIP3*. The strongest (probability of observing and pathogenic) of these non-sequenced variants was `p.Cys243Arg` (posterior: 0.347). However, the total probability of a causal diagnosis for the patient *given the available evidence* was 0 (95% CI: 0–0) since these missing variants must be accounted for (**Table S3**). Upon confirmation, these probabilities can update, as per scenario two.

3.6 Posterior probabilities are calculated across all qualifying variants

While only the top-ranked gene/variant is shown in each of the three scenarios, we emphasise that the same posterior probability and CrI calculations are performed across all plausible candidates. In real-world diagnostics, we commonly find multiple variants to carry non-negligible probabilities. Our framework explicitly quantifies these competing hypotheses, enabling a ranked interpretation that reflects the totality of evidence. Overlapping CrI do not indicate ambiguity in the method, but rather a principled measure of remaining uncertainty. This output can directly inform follow-up actions, such as functional validation or treatment trials, and supports the use of CrI thresholds as a transparent decision-making aid when data are incomplete or

equivocal.

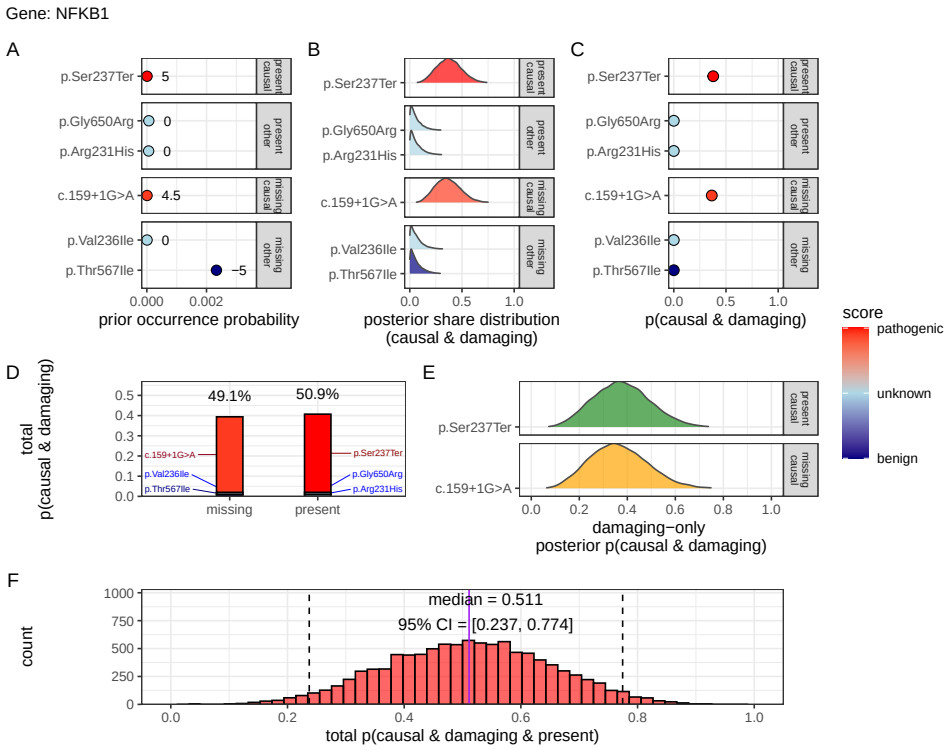

Figure 2: **Quantification of present (TP) and missing (FN) causal genetic variants for disease in *NFKB1* (scenario 2).** The example proband carried three known heterozygous variants, including pathogenic `p.Ser237Ter`, and had incomplete coverage at three additional loci, including likely-pathogenic splice-site variant `c.159+1G>A`. The sequential steps towards the posterior probability of complete genetic diagnosis are shown: (A) Prior occurrence probabilities, stratified by observed/missing and causal/non-causal status. Pathogenicity scores (-5 to +5) are annotated. (B) Posterior distributions of normalised variant weights $\tilde{\pi}_i$. (C) Per-variant posterior probability of being both damaging and causal. (D) Posterior distributions for causal variants only. (E) Decomposition of total pathogenic probability into observed (green) and missing (orange) sources. (F) Gene-level posterior showing the probability that at least one damaging causal allele is present; median 0.54, 95 % CrI 0.26-0.80. This result can be compared to scenarios one and three in **Figures S2** and **S3**, respectively.

3.7 Validation studies

3.7.1 Validation of dominant disease occurrence with *NFKB1*

To validate our genome-wide probability estimates for AD disorders, we focused on *NFKB1*. We used a reference dataset from Tuijnenburg et al. (19), in which whole-

genome sequencing of 846 PID patients identified *NFKB1* as one of the genes most strongly associated with the disease, with 16 *NFKB1*-related CVID cases attributed to AD heterozygous variants. Our goal was to compare the predicted number of *NFKB1*-related CVID cases with the reported count in this well-characterised national-scale cohort.

Our model calculated 0 known pathogenic variant *NFKB1*-related CVID cases in the UK with a minimal risk of 456 unknown de novo variants. In the reference cohort, 16 *NFKB1* CVID cases were reported. We additionally wanted to account for potential under-reporting in the reference study. We used an extrapolated national CVID prevalence which yielded a median estimate of 118 cases (95% CI: 70–181), while a Bayesian-adjusted mixture estimate produced a median of 67 cases (95% CI: 43–99). **Figure S5 (A)** illustrates that our predicted values reflect these ranges and are closer to the observed count. This case supports the validity of our integrated probability estimation framework for AD disorders, and represents a challenging example where pathogenic SNV are not reported in the reference population of gnomAD. Our min-max values successfully contained the true reported values.

3.7.2 Validation of recessive disease occurrence with *CFTR*

Our analysis predicted the number of CF cases attributable to carriage of the `p.Arg117His` variant (either as homozygous or as compound heterozygous with another pathogenic allele) in the UK. Based on HWE calculations and mortality adjustments, we predicted approximately 648 cases arising from biallelic variants and 160 cases from homozygous variants, resulting in a total of 808 expected cases.

In contrast, the nationally reported number of CF cases was 714, as recorded in the UK Cystic Fibrosis Registry 2023 Annual Data Report (23). To account for factors such as reduced penetrance and the mortality-adjusted expected genotype, we derived a Bayesian-adjusted estimate via posterior simulation. Our Bayesian approach yielded a median estimate of 740 cases (95% Confidence Interval (CI): 696, 786) and a mixture-based estimate of 727 cases (95% CI: 705, 750). **Figure S5 (B)** illustrates the close concordance between the predicted values, the Bayesian-adjusted estimates, and the national report supports the validity of our approach for estimating disease.

Figure S4 shows the final values for these genes of interest in a given population size and phenotype. It reveals that an allele frequency threshold of approximately 0.000007 is required to observe a single heterozygous carrier of a disease-causing variant in the UK population for both genes. However, owing to the AR MOI pattern of *CFTR*, this threshold translates into more than 100,000 heterozygous carriers, compared to only 456 carriers for the AD gene *NFKB1*. Note that this allele frequency threshold, being derived from the current reference population, represents a lower bound that can become more precise as public datasets continue to grow. This marked difference underscores the significant impact of MOI patterns on population carrier frequencies and the observed disease prevalence.

3.7.3 Interpretation of ClinVar variant occurrences

Figure S6 shows the two validation study PID genes, representing AR and dominant MOI. **Figure S6 (A)** illustrates the overall probability of an affected birth by ClinVar variant classification, whereas **Figure S6 (B)** depicts the total expected number of cases per classification for an example population, here the UK, of approximately 69.4 million.

3.7.4 Validation of SCID-specific disease occurrence

Given that SCID is a subset of PID, our probability estimates reflect the likelihood of observing a genetic variant as a diagnosis when the phenotype is PID. However, we additionally tested our results against SCID cohorts in **Figure S8**. The summarised raw cohort data for SCID-specific gene counts are summarised and compared across countries in **Figure S7**. True counts for *IL2RG* and *DCLRE1C* from ten distinct locations yielded 95% CI surrounding our predicted values. For *IL2RG*, the prediction was low (approximately 1 case per 1,000,000 PID), as expected since loss-of-function variants in this XL gene are highly deleterious and rarely observed in gnomAD. In contrast, the predicted value for *RAG1* was substantially higher (553 cases per 1,000,000 PID) than the observed counts (ranging from 0 to 200). We attributed this discrepancy to the lower penetrance and higher background frequency of *RAG1* variants in recessive inheritance, whereby reference studies may underreport the true national incidence. Overall, we report that agreement within an order of magnitude was tolerable given the inherent uncertainties from reference studies arising from variable penetrance and allele frequencies.

3.8 Application to inborn errors of immunity

3.8.1 Genetic constraint in high-impact protein networks

We next applied our framework to IEI, a disease area in which we have expertise and which offers a well-curated gene set to validate genome-wide estimates and demonstrate potential applications (14).

Given that pathogenicity in IEI may reflect shared molecular pathways, we integrated ClinVar-derived variant probability estimates with PPI data to quantify pathogenic burden per gene and examine whether genetic constraint aggregates within specific networks and corresponds to established IEI classifications and immunophenotypes (4; 17).

3.8.2 Score-positive-total within IEI PPI network

The ClinVar classifications reported in **Figure 1** were scaled -5 to +5 based on their pathogenicity. We were interested in positive (potentially damaging) but not

negative (benign) scoring variants, which are statistically incidental in this analysis. We tallied gene-level positive scores to give the score-positive-total metric. **Figure S9 (A)** shows the PPI network of disease-associated genes, where node size and colour encode the score-positive-total (log-transformed). The top 15 genes with the highest total prior probabilities of being observed with disease are labelled (as per **Figure 1**).

3.8.3 Association analysis of score-positive-total across IEI categories

We checked for any statistical enrichment in score-positive-totals, which represents the expected observation of pathogenicity, between the IEI categories. One-way ANOVA revealed an effect of major disease category on score-positive-total ($F(8, 500) = 2.82$, $p = 0.0046$), indicating that group means were not identical, which we observed in **Figure S9 (B)**. However, despite some apparent differences in median scores across categories (i.e. 9. Bone Marrow Failure (BMF)), the Tukey HSD post hoc comparisons **Figure S9 (C)** showed that all pairwise differences had 95% CIs overlapping zero, suggesting that individual group differences were not significant.

3.8.4 UMAP embedding of the PPI network

To address the density of the PPI network for the IEI gene panel, we applied UMAP (**Figure 3**). Node sizes reflect interaction degree, a measure of evidence-supported connectivity (17). We tested for a correlation between interaction degree and score-positive-total. In **Figure 3**, gene names with degrees above the 95th percentile are labelled in blue, while the top 15 genes by score-positive-total are labelled in yellow (as per **Figure 1**). Notably, genes with high pathogenic variant loads segregated from highly connected nodes, suggesting that LOF in hub genes is selectively constrained, whereas damaging variants in lower-degree genes yield more specific effects. This observation was subsequently tested empirically.

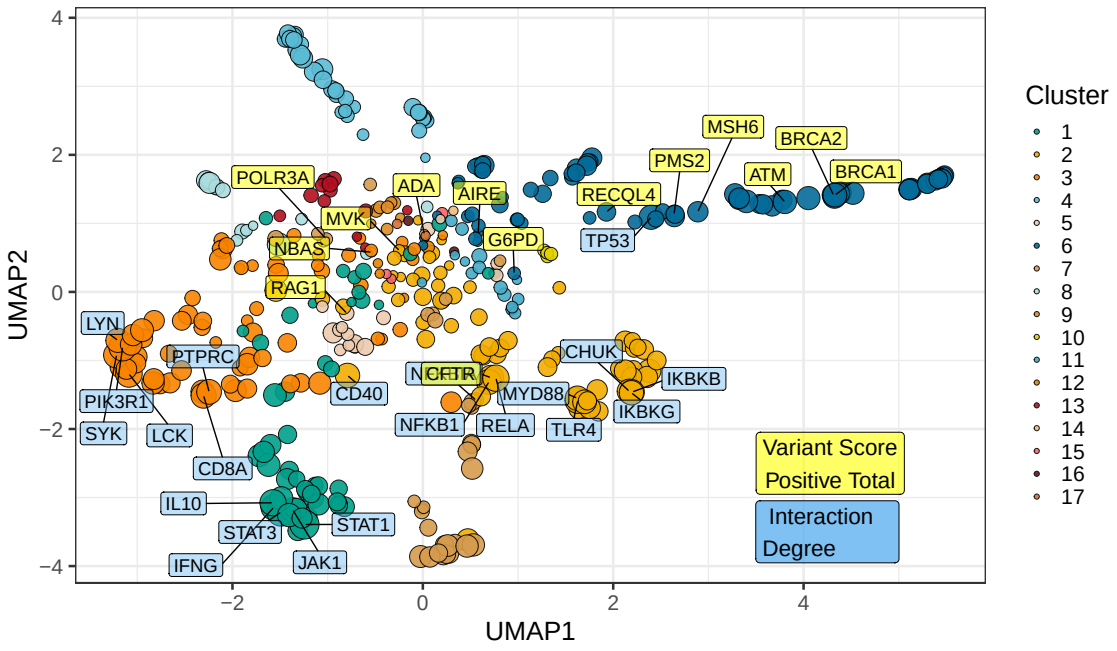

Figure 3: **UMAP embedding of the PPI network.** The plot projects the high-dimensional protein-protein interaction network into two dimensions, with nodes coloured by cluster and sized by interaction degree. Blue labels indicate hub genes (degree above the 95th percentile) and yellow labels mark the top 15 genes by score-positive-total (damaging ClinVar classifications). The spatial segregation suggests that genes with high pathogenic variant loads are distinct from highly connected nodes.

3.8.5 Hierarchical clustering of enrichment scores for major disease categories

Figure S10 presents a heatmap of standardised residuals for major disease categories across network clusters, as per **Figure 3**. A dendrogram clusters similar disease categories, while the accompanying bar plot displays the maximum absolute standardised residual for each category. Notably, (8) Complement Deficiencies (CD) shows the highest maximum enrichment, followed by (9) BMF. While all maximum values exceed 2, the threshold for significance, this likely reflects the presence of protein clusters with strong damaging variant scores rather than uniform significance across all categories (i.e. genes from cluster 4 in 8 CD).

3.8.6 PPI connectivity, LOEUF constraint and enriched network cluster analysis

Based on the preliminary insight from **Figure S10**, we evaluated the relationship between network connectivity (PPI degree) and LOF constraint (LOEUF upper rank) Karczewski et al. (4) using Spearman's rank correlation. Overall, there was a weak

but significant negative correlation ($\rho = -0.181$, $p = 0.00024$) at the global scale, indicating that highly connected genes tend to be more constrained. A supplementary analysis (**Figure S11**) did not reveal distinct visual associations between network clusters and constraint metrics, likely due to the high network density. However once stratified by gene clusters, the natural biological scenario based on quantitative PPI evidence (17), some groups showed strong correlations; for instance, cluster 2 ($\rho = -0.375$, $p = 0.000994$) and cluster 4 ($\rho = -0.800$, $p < 0.000001$), while others did not. This indicated that shared mechanisms within pathway clusters may underpin genetic constraints, particularity for LOF intolerance. We observe that the score-positive-total metric effectively summarises the aggregate pathogenic burden across IEI genes, serving as a robust indicator of genetic constraint and highlighting those with elevated disease relevance.

Figure S12 (C, D) shows the re-plotted PPI networks for clusters with significant correlations between PPI degree and LOEUF upper rank. In these networks, node size is scaled by a normalised variant score, while node colour reflects the variant score according to a predefined palette.

3.8.7 New insight from functional enrichment

To interpret the functional relevance of our prioritised IEI gene sets with the highest load of damaging variants (i.e. clusters 2 and 4 in **Figure S12**), we performed functional enrichment analysis for known disease associations using MsigDB with FUMA (i.e. GWAScatalog and Immunologic Signatures) (26). Composite enrichment profiles (**Figure S13**) reveal that our enriched PPI clusters were associated with distinct disease-related phenotypes, providing functional insights beyond traditional IUIS IEI groupings (14). The gene expression profiles shown in **Figure S14** (GTEx v8 54 tissue types) offer the tissue-specific context for these associations. Together, these results enable the annotation of IEI gene sets with established disease phenotypes, supporting a data-driven classification of IEI.

Based on these independent sources of interpretation, we observed that genes from cluster 2 were independently associated with specific inflammatory phenotypes, including ankylosing spondylitis, psoriasis, inflammatory bowel disease, and rheumatoid arthritis, as well as quantitative immune traits such as lymphocyte and neutrophil percentages and serum protein levels. In contrast, genes from cluster 4 were linked to ocular and complement-related phenotypes, notably various forms of age-related macular degeneration (e.g. geographic atrophy and choroidal neovascularisation) and biomarkers of the complement system (e.g. C3, C4, and factor H-related proteins), with additional associations to nephropathy and pulmonary function metrics.

3.8.8 Genome-wide gene distribution and linkage disequilibrium

Figure 4 (A) shows a genome-wide karyoplot of all IEI panel genes across GRCh38, with colour-coding based on MOI. Figures **(B)** and **(C)** display zoomed-in locus plots

for *NFKB1* and *CFTR*, respectively. In **Figure 4 (B)**, the probability of observing variants with known classifications is high only for variants such as p.Ala475Gly, which are considered benign in the AD *NFKB1* gene that is intolerant to LOF. In **Figure 4 (C)**, high probabilities of observing patients with pathogenic variants in *CFTR* are evident, reproducing this well-established phenomenon. Furthermore, the analysis of Linkage Disequilibrium (LD) using R^2 shows that high LD regions can be modelled effectively, allowing independent variant signals to be distinguished.

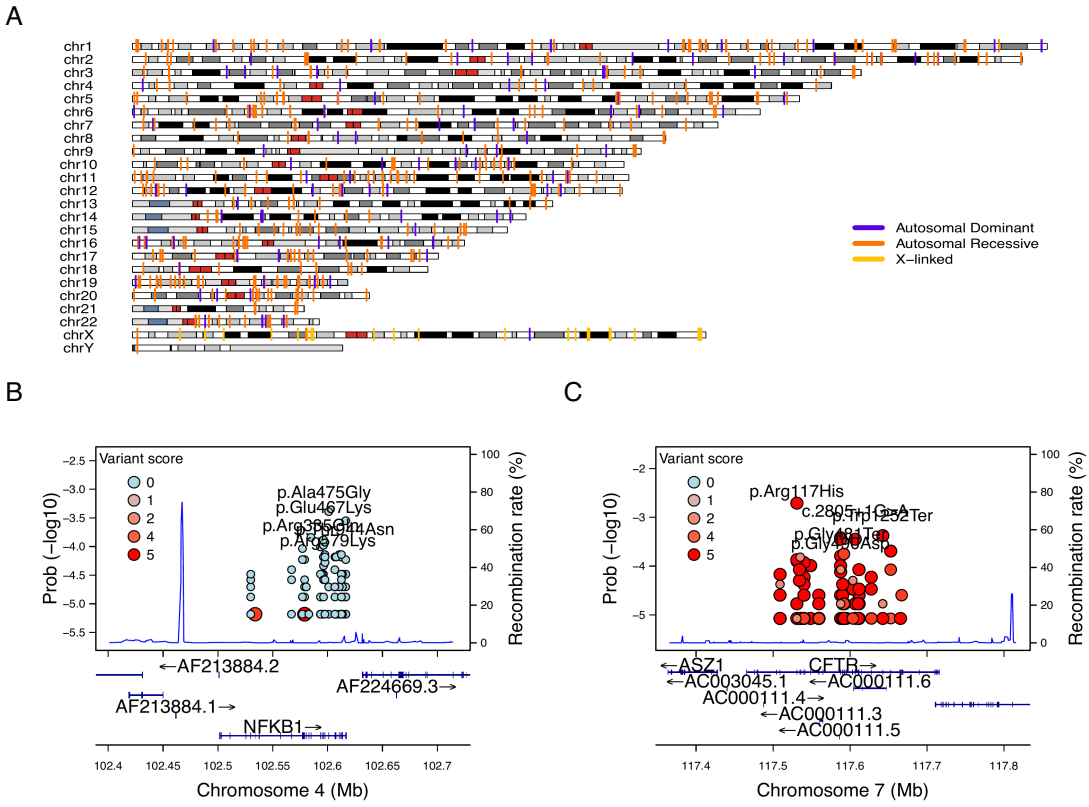

Figure 4: **Genome-wide IEI, variant occurrence probability and LD by R^2.** (A) Genome-wide karyoplot of all IEI panel genes mapped to GRCh38, with colours indicating MOI. (B) Zoomed-in locus plot example for *NFKB1* showing variant occurrence probabilities; only benign variants such exhibit high probabilities in this AD gene intolerant to LOF. (C) Locus plot example for *CFTR* displaying high probabilities for pathogenic variants; due to the dense clustering of pathogenic variants, score filter >0 was applied. Top five variants are labelled per gene.

3.8.9 Novel PID classifications derived from genetic PPI and clinical features

We recategorised 315 immunophenotypic features from the original IUIS IEI annotations, reducing detailed descriptions (e.g. “decreased CD8, normal or decreased CD4”)

to minimal labels (e.g. "low") and then binarising them (normal vs. not-normal) for T cells, B cells, Immunoglobulin (Ig) and neutrophils (**Figure S15**). These simplified profiles were mapped onto STRINGdb PPI clusters, revealing non-random distributions ($\chi^2 <$ 1e-13; **Figure S16**), indicating that network context captures key immunophenotypic variation.

We next compared four classifiers under 5-fold cross-validation to determine which features predicted PPI clustering. As shown in **Figure S17**, the fully combined model achieved the highest accuracy among the four: (i) phenotypes only (33 %) (i.e. T cell, B cell, Ig, Neutrophil); (ii) phenotypes + IUIS major category (50 %) (e.g. CID. See **Box 2.1** for more); (iii) IUIS major + subcategory only (59 %) (e.g. CID, T-B+ SCID); and (iv) phenotypes + IUIS major + subcategory (61 %). This demonstrated that incorporating both traditional IUIS IEI classifications and core immunophenotypic markers into the PPI-based framework yielded the most robust discrimination of PID gene clusters. Variable importance analysis highlighted abnormality status for Ig and T cells were among the top ten features in addition to the other IUIS major and sub categories. Per-class specificity remained uniform across the classes while sensitivity dropped.

The PPI and immunophenotype model yielded 17 data-driven PID groups, whereas incorporating the full complement of IUIS categories expanded this to 33 groups. For clarity, we only demonstrate the decision tree from the smaller 17-group model in **Figure 5**. Each terminal node is annotated by its predominant immunophenotypic signature (for example, "group 65 with abnormal T cell and B cell features"), and the full resulting gene counts per 33 class are plotted in **Figure 5**. Although, less user-friendly, this data-driven taxonomy both aligns with and refines traditional IUIS IEI classifications to provide a scaffold for large-scale computational analyses. Because this framework is fully reproducible, alternative PPI embeddings that incorporate additional molecular annotations can readily swapped to continue building on these IEI classification schemes.

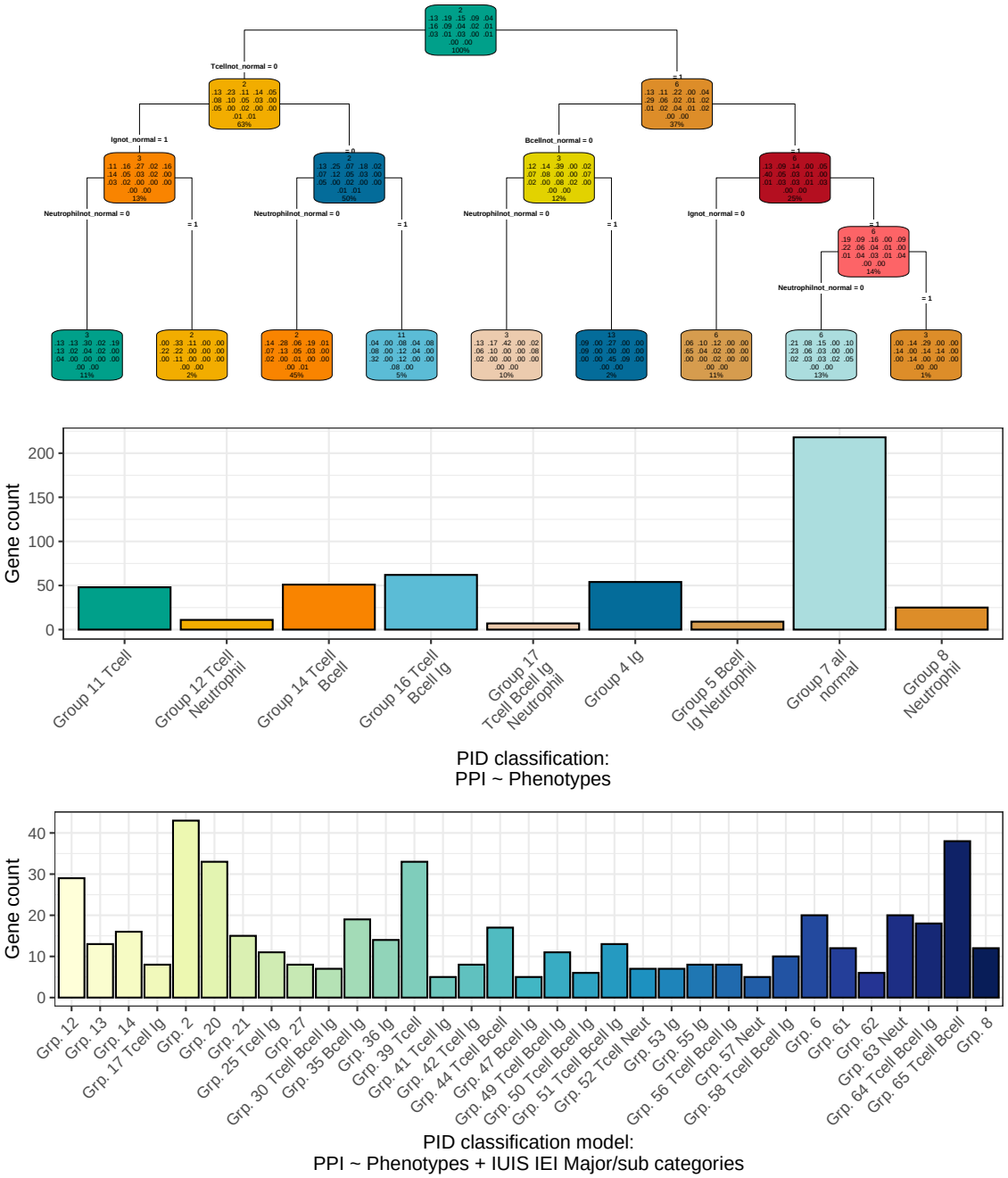

Figure 5: **Fine-tuned model for PID classification.** (Top) In each terminal node, the top block indicates the number of genes in the node; the middle block shows the fitted class probabilities (which sum to 1); and the bottom block displays the percentage of the total sample in that node. These metrics summarise the model's assignment based on immunophenotypic and PPI features. (Middle) Bar plot presenting the distribution of novel PID classifications, where group labels denote the predominant abnormal clinical feature(s) (e.g. T cell, B cell, Ig, Neutrophil) characterising each group. (Bottom) The complete model including the traditional IUIS IEI categories.

3.9 Probability of observing AlphaMissense pathogenicity

AlphaMissense provides pathogenicity scores for all possible amino acid substitutions; however, our results in **Figure 6** show that the most probable observations in patients occur predominantly for benign or unknown variants. This finding places the likelihood of disease-associated substitutions into perspective and offers a data-driven foundation for future improvements in variant prediction. The values in **Figure 6 (A)** can be directly compared to **Figure 1 (D)** to view the distribution of classifications. A Kruskal-Wallis test was used to compare the observed disease probability across clinical classification groups and no significant differences were detected. In general, most variants in patients are classified as benign or unknown, indicating limited discriminative power in the current classification, such that pathogenicity prediction does not infer occurrence prediction (**Figure S18**). Inverse correlation likely depends on factors like MOI and intolerance to LOF.

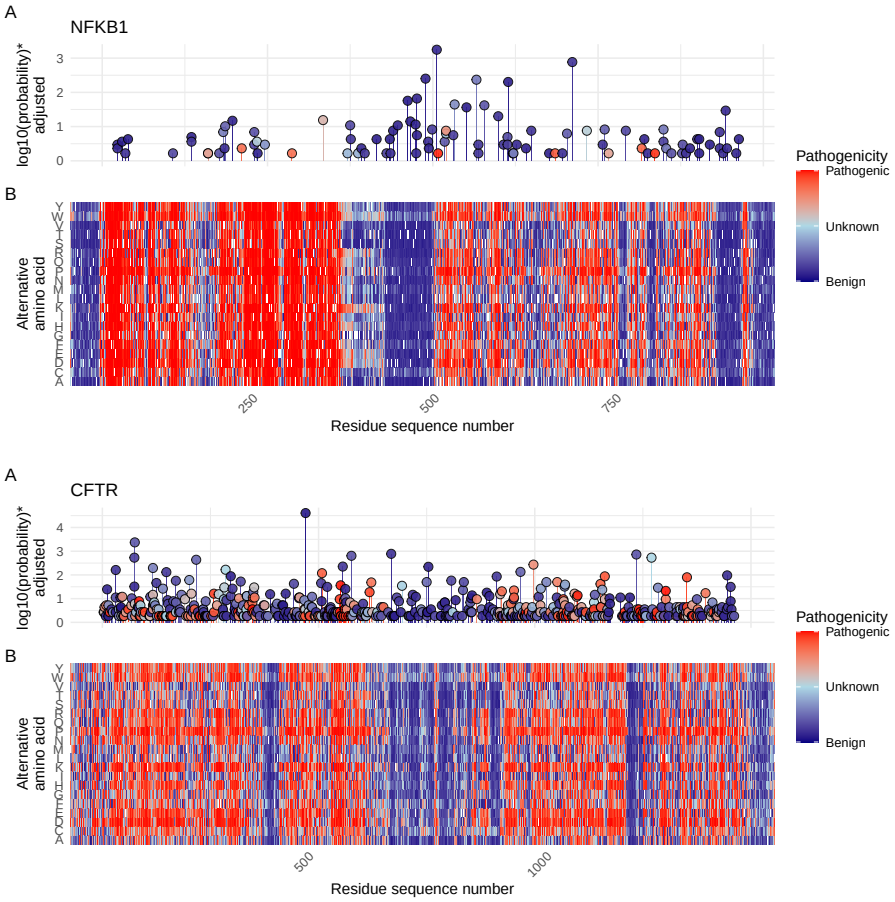

Figure 6: **(A) Probabilities of observing a patient with (B) AlphaMissense-derived pathogenicity scores.** Although AlphaMissense provides scores for every possible amino acid substitution, the most frequently observed variants in patients tend to be classified as benign or of unknown significance. This juxtaposition contextualises the likelihood of disease-associated substitutions and underlines prospects for refining predictive models. *Axis scaling for visibility near zero. Higher point indicates higher probability.

3.10 Integration of variant probabilities into IEI genetics data

We integrated the computed prior probabilities for observing variants in all known genes associated with a given phenotype (14), across AD, AR, and XL MOI, into our IEI genetics framework. These calculations, derived from gene panels in PanelAppRex, have yielded novel insights for the IEI disease panel. The final result comprised of machine- and human-readable datasets, including the table of variant classifications and priors available via a the linked repository (28), and a user-friendly web interface that incorporates these new metrics.

Figure 7 shows the interface summarising integrated variant data. We include pre-calculated summary statistics and clinical significance as numerical metrics. Key quantiles (min, Q1, median, Q3, max) for each gene are rendered as sparkline box plots, and dynamic URLs link table entries to external databases (e.g. ClinVar, Online Mendelian Inheritance in Man (OMIM), AlphaFold) as per **Section 3.1**. The prepared data are available for bioinformatic application (28) as per **Section 3.2**.

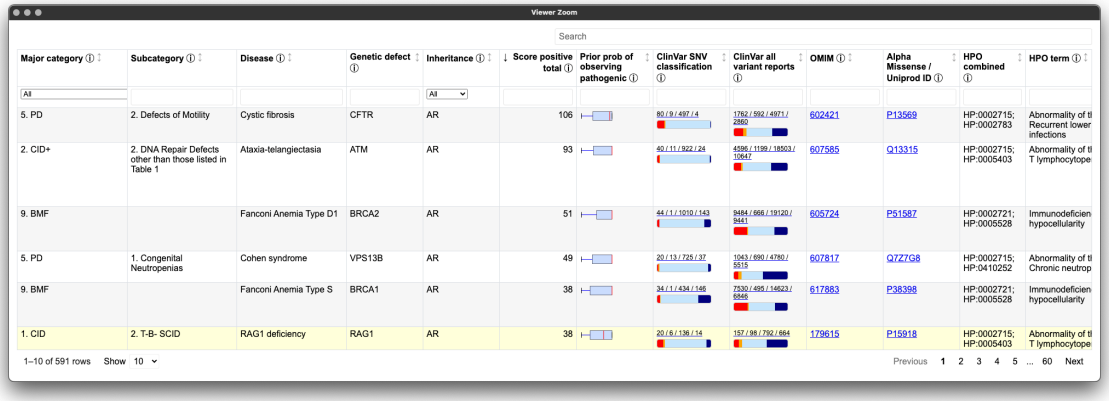

Figure 7: **Integration of variant probabilities into the IEI genetics framework.** The interface summarises the condensed variant data, with pre-calculated summary statistics and dynamic links to external databases. This integration enables immediate access to detailed variant classifications and prior probabilities for each gene.

4 Discussion

Our study presents, to our knowledge, the first comprehensive framework for calculating prior probabilities of observing disease-associated variants and the first to demonstrate the method for an evidence-aware genetic diagnosis with CrI (5; 7). By integrating large-scale genomic annotations, including population allele frequencies from gnomAD (4), variant classifications from ClinVar (10), and functional annotations from resources such as dbNSFP, with classical HWE-based calculations, we derived robust estimates for 54,814 ClinVar variant classifications across 557 IEI genes implicated in PID and monogenic inflammatory bowel disease (12; 14). Although our results focus on IEI, the genome-wide framework also supports all inheritance patterns: AD and XL require a single pathogenic allele, whereas AR demands homozygous or compound heterozygous states. Classical HWE-based estimates thus furnish baseline occurrence probabilities and serve as robust priors for Bayesian risk models, a practice underutilised until the advent of large-scale databases (4; 9; 10; 12).

A major deficit in current clinical genetics is the prevailing focus on confirming only the presence of TP variants. Our approach yielded three key results to overcome this hurdle. We generated per-variant priors across all MOI. The patient's results of observed and unobserved variants were integrated into a single posterior probability of carrying a damaging causal allele. As demonstrated in **Table S2** and **Figure 2**, this key result delivers a clinically applicable, interpretable probability that combines both detected and potentially unobserved variants. When whole-genome sequencing analyses are not yet available, the score-positive-total metric can serve as an optional decision aid, enabling manual, evidence-based ranking of candidate genes to prioritise diagnoses in patients with overlapping phenotypes.

We acknowledge that our framework is currently focused (but not restricted) on SNVs and does not incorporate numerous other complexities of genetic disease, such as structural variants, de novo variants, hypomorphic alleles, overdominance, variable penetrance, tissue-specific expression, the Wahlund effect, pleiotropy, and others (3). In certain applications, more refined estimates would benefit from including factors such as embryonic lethality, condition-specific penetrance, and age of onset (7). Our analysis also relies on simplifying assumptions of random mating, an effectively infinite population, and the absence of migration, novel mutations, or natural selection. We demonstrated the genome-wide gene distribution and MOI for the IEI panel relative to LD showing that it is an important consideration and is feasible. However, LD is a challenging feature that requires accurate implementation which depends on the whole genome population-based pairwise genotype matrices for the given population. We used the reference global population AFs, which is more generalisable but less accurate than population-specific AF values.

In the example single-case diagnosis scenarios, our approach enabled high-confidence attribution to a known pathogenic variant while also capturing the potential impact of a likely-pathogenic splice-site allele that was missed by sequencing. Scenario two showed a common diagnostic challenge where a strong candidate exists alongside an

unconfirmed but plausible alternative. Our method distributes confidence across both possibilities. Conventional approaches focus only on detecting TP and cannot provide this insight. By quantifying residual uncertainty, we can generate structured reports that clearly distinguish supported, excluded, and plausible-but-unseen variants. We call this "evidence-aware" interpretation. When combined with genome-wide priors from the full range of disease-gene panels, this approach applies to any phenotype from PanelAppRex. By combining variant classification, allele frequency, MOI, and sequencing quality metrics, our method creates a scalable foundation for evidence-aware diagnostics in clinical genomics.

Estimating disease risk in genetic studies is complicated by uncertainties in key parameters such as variant penetrance and the fraction of cases attributable to specific variants (3). In the simplest model, where a single, fully penetrant variant causes disease, the lifetime risk $P(D)$ is equivalent to the genotype frequency $P(G)$. For an allele with frequency p (ignoring LD for AR), this translates to:

$$\begin{aligned} \text{Autosomal Recessive:} \quad & P(D) = p^2, \\ \text{Autosomal Dominant:} \quad & P(D) = 2p(1-p) \approx 2p. \end{aligned}$$

When penetrance is incomplete, defined as $P(D \mid G)$, the risk becomes: $P(D) = P(G)\,P(D \mid G)$. In more realistic scenarios where multiple variants contribute to disease, $P(G \mid D)$ denotes the fraction of cases attributable to a given variant. This leads to:

$$P(D) = \frac{P(G)\,P(D \mid G)}{P(G \mid D)}.$$

Because both penetrance and $P(G \mid D)$ are often uncertain, solving this equation systematically poses a major challenge, which we incidentally tackled in the validation studies (29; 30).

Our framework addresses this challenge by combining variant classifications, population allele frequencies, and curated gene-disease associations. While imperfect on an individual level, these sources exhibit predictable aggregate behaviour, supported by James-Stein estimation principles (31). Curated gene-disease associations help identify genes that are explainable for most disease cases, allowing us to approximate $P(G \mid D)$ close to one. In this way, we obtain robust estimates of $P(G)$ (the frequency of disease-associated genotypes), even when exact values of penetrance and case attribution remain uncertain.

This approach allows us to pre-calculate priors and summarise the overall pathogenic burden. By focusing on a subset $\mathcal{V}$ of variants that pass stringent filtering, where each $P(G_i \mid D)$ is the probability that a case of disease D is attributable to variant(s) i, we assume that, in aggregate,

$$\sum_{i \in \mathcal{V}} P(G_i \mid D) \approx 1.$$

Even if the cumulative contribution is slightly less than one, the resultant risk estimates remain robust within the broad CrIs typical of epidemiological studies. By incorporating these pre-calculated priors into a Bayesian framework, our method refines risk estimates and enhances clinical decision-making despite inherent uncertainties.

For the IEI-specific investigation, we showed that immunophenotypic and network-derived features can be used to train and test models that predict PPIs. From this, we derived a new, simplified classification of immune features for IEI genes. We have listed the new immunophenotypic categories (e.g. T cell low) in the user database, however we have not included the detailed cluster assignments (e.g. PPI groups) because they are too complex for direct interpretation manually. Instead, our demonstration provides worked examples that bioinformaticians can use to perform more refined clustering in larger studies.

Moreover, because variant sets can be collapsed instead of relying on the gene-level, our method complements existing statistical approaches for aggregating variant effects with methods like Sequence Kernel Association Test (SKAT) and Aggregated Cauchy Association Test (ACAT) (32–35) and multi-omics integration techniques (36; 37). It also remains consistent with established variant interpretation guidelines from the American College of Medical Genetics and Genomics (ACMG) (38) and complementary frameworks (39; 40), as well as QC protocols (41; 42). Standardised reporting for qualifying variant sets, such as ACMG Secondary Findings v3.2 (43), further contextualises the integration of these probabilities into clinical decision-making.

We compared our occurrence probabilities with AlphaMissense pathogenicity scores and observed that common variants are predominantly scored as benign or of uncertain significance. While this aligns with their allele frequencies, any pathogenic variant seen in a patient warrants evaluation against its prior observation probability to assess causality. Predictive tools such as AlphaMissense could ostensibly enhance their embedding of variant features by incorporating gene-disease associations and MOI data, which may not be fully represented by raw population allele frequencies.

Future work should incorporate the additional variant types and models to further refine these probability estimates. By continuously updating classical estimates with emerging data and prior knowledge, we aim to enhance the precision of genetic diagnostics and ultimately improve patient care.

5 Conclusion

We present a statistical framework that resolves the long-standing challenge of quantifying the probability that any candidate variant is causal for genetic disease. Unlike traditional methods that stop at pathogenic or benign labels, our approach integrates both observed variants and the possibility of unobserved causal alleles into a single probabilistic model. By combining classical population genetics, large-scale variant data, and Bayesian inference, we generate genome-wide priors across inheritance modes and provide credible intervals that reflect both evidence and residual uncertainty. Although demonstrated here in inborn errors of immunity, the framework is broadly applicable and establishes a quantitative foundation for variant interpretation, clinical decision-making, and future genomic analyses.

Acknowledgements

We would like to thank all the patients and families who have been providing advice on SwissPedHealth and its projects, as well as the clinical and research teams at the participating institutions. We acknowledge Genomics England for providing public access to the PanelApp data. The use of data from Genomics England panelapp was licensed under the Apache License 2.0. The use of data from UniProt was licensed under Creative Commons Attribution 4.0 International (CC BY 4.0). ClinVar asks its users who distribute or copy data to provide attribution to them as a data source in publications and websites (10). dbNSFP version 4.4a is licensed under the Creative Commons Attribution-NonCommercial-NoDerivatives 4.0 International (CC BY-NC-ND 4.0); while we cite this dataset as used our research publication, it is not used for the final version which instead used ClinVar and gnomAD directly. GnomAD is licensed under Creative Commons Zero Public Domain Dedication (CC0 1.0 Universal). GnomAD request that usages cites the gnomAD flagship paper (4) and any online resources that include the data set provide a link to the browser, and note that tool includes data from the gnomAD v4.1 release. AlphaMissense asks to cite Cheng et al. (9) for usage in research, with data available from Cheng et al. (18).

Contributions

DL performed main analyses and wrote the manuscript. SB, AS, MS, and JT designed analysis and wrote the manuscript. JF, LJS supervised the work, and applied for funding. The Quant Group is a collaboration across multiple institutions where authors contribute equally; the members on this project were DL, SB, AS, and MS.

Competing interest

The authors declare no competing interest.

Ethics statement

This study only used data which was previously published and publicly available, as cited in the manuscript. This SwissPedHealth study, under which this work was carried out, was approved based on the advice of the ethical committee Northwest and Central Switzerland (EKNZ, AO_2022-00018). The study was conducted in accordance with the Declaration of Helsinki.

Funding

This project was supported through the grant Swiss National Science Foundation (SNF) 320030_201060, and NDS-2021-911 (SwissPedHealth) from the Swiss Personalized Health Network and the Strategic Focal Area 'Personalized Health and Related Technologies' of the ETH Domain (Swiss Federal Institutes of Technology).

References

[1] Oliver Mayo. A Century of Hardy–Weinberg Equilibrium. *Twin Research and Human Genetics*, 11(3):249–256, June 2008. ISSN 1832-4274, 1839-2628. doi: 10.1375/twin.11.3.249. URL https://www.cambridge.org/core/product/identifier/S1832427400009051/type/journal_article.

[2] Nikita Abramovs, Andrew Brass, and May Tassabehji. Hardy-Weinberg Equilibrium in the Large Scale Genomic Sequencing Era. *Frontiers in Genetics*, 11:210, March 2020. ISSN 1664-8021. doi: 10.3389/fgene.2020.00210. URL https://www.frontiersin.org/article/10.3389/fgene.2020.00210/full.

[3] Johannes Zschocke, Peter H. Byers, and Andrew O. M. Wilkie. Mendelian inheritance revisited: dominance and recessiveness in medical genetics. *Nature Reviews Genetics*, 24(7):442–463, July 2023. ISSN 1471-0056, 1471-0064. doi: 10.1038/s41576-023-00574-0. URL https://www.nature.com/articles/s41576-023-00574-0.

[4] Konrad J Karczewski, Laurent C Francioli, Grace Tiao, Beryl B Cummings, Jessica Alföldi, Qingbo Wang, Ryan L Collins, Kristen M Laricchia, Andrea Ganna, Daniel P Birnbaum, et al. The mutational constraint spectrum quantified from variation in 141,456 humans. *Nature*, 581(7809):434–443, 2020.

[5] Sarah L. Bick, Aparna Nathan, Hannah Park, Robert C. Green, Monica H. Wojcik, and Nina B. Gold. Estimating the sensitivity of genomic newborn screening for treatable inherited metabolic disorders. *Genetics in Medicine*, 27(1): 101284, January 2025. ISSN 10983600. doi: 10.1016/j.gim.2024.101284. URL https://linkinghub.elsevier.com/retrieve/pii/S1098360024002181.

[6] Benjamin D. Evans, Piotr Słowiński, Andrew T. Hattersley, Samuel E. Jones, Seth Sharp, Robert A. Kimmitt, Michael N. Weedon, Richard A. Oram, Krasimira Tsaneva-Atanasova, and Nicholas J. Thomas. Estimating disease prevalence in large datasets using genetic risk scores. *Nature Communications*, 12(1):6441, November 2021. ISSN 2041-1723. doi: 10.1038/s41467-021-26501-7. URL https://www.nature.com/articles/s41467-021-26501-7.

[7] William B. Hannah, Mitchell L. Drumm, Keith Nykamp, Tiziano Pramparo, Robert D. Steiner, and Steven J. Schrodi. Using genomic databases to determine the frequency and population-based heterogeneity of autosomal recessive conditions. *Genetics in Medicine Open*, 2:101881, 2024. ISSN 29497744. doi: 10.1016/j.gimo.2024.101881. URL https://linkinghub.elsevier.com/retrieve/pii/S2949774424010276.

[8] John Jumper, Richard Evans, Alexander Pritzel, Tim Green, Michael Figurnov, Olaf Ronneberger, Kathryn Tunyasuvunakool, Russ Bates, Augustin Žídek, Anna Potapenko, Alex Bridgland, Clemens Meyer, Simon A. A. Kohl, Andrew J. Ballard, Andrew Cowie, Bernardino Romera-Paredes, Stanislav Nikolov, Rishub Jain, Jonas Adler, Trevor Back, Stig Petersen, David Reiman, Ellen Clancy, Michal Zielinski, Martin Steinegger, Michalina Pacholska, Tamas Berghammer, Sebastian Bodenstein, David Silver, Oriol Vinyals, Andrew W. Senior, Koray Kavukcuoglu, Pushmeet Kohli, and Demis Hassabis. Highly accurate protein structure prediction with AlphaFold. *Nature*, 596(7873):583–589, August 2021. ISSN 0028-0836, 1476-4687. doi: 10.1038/s41586-021-03819-2. URL https://www.nature.com/articles/s41586-021-03819-2.

[9] Jun Cheng, Guido Novati, Joshua Pan, Clare Bycroft, Akvilė Žemgulytė, Taylor Applebaum, Alexander Pritzel, Lai Hong Wong, Michal Zielinski, Tobias Sargeant, Rosalia G. Schneider, Andrew W. Senior, John Jumper, Demis Hassabis, Pushmeet Kohli, and Žiga Avsec. Accurate proteome-wide missense variant effect prediction with AlphaMissense. *Science*, 381(6664):eadg7492, September 2023. ISSN 0036-8075, 1095-9203. doi: 10.1126/science.adg7492. URL https://www.science.org/doi/10.1126/science.adg7492.

[10] Melissa J Landrum, Jennifer M Lee, Mark Benson, Garth R Brown, Chen Chao, Shanmuga Chitipiralla, Baoshan Gu, Jennifer Hart, Douglas Hoffman, Wonhee Jang, Karen Karapetyan, Kenneth Katz, Chunlei Liu, Zenith Maddipatla, Adriana Malheiro, Kurt McDaniel, Michael Ovetsky, George Riley, George Zhou, J Bradley Holmes, Brandi L Kattman, and Donna R Maglott. ClinVar: improving access to variant interpretations and supporting evidence. *Nucleic Acids*

Research, 46(D1):D1062–D1067, January 2018. ISSN 0305-1048, 1362-4962. doi: 10.1093/nar/gkx1153. URL http://academic.oup.com/nar/article/46/D1/D1062/4641904.

[11] The UniProt Consortium, Alex Bateman, Maria-Jesus Martin, Sandra Orchard, Michele Magrane, Aduragbemi Adesina, Shadab Ahmad, Bowler-Barnett, and Others. UniProt: the Universal Protein Knowledgebase in 2025. *Nucleic Acids Research*, 53(D1):D609–D617, January 2025. ISSN 0305-1048, 1362-4962. doi: 10.1093/nar/gkae1010. URL https://academic.oup.com/nar/article/53/D1/D609/7902999.

[12] Dylan Lawless. PanelAppRex aggregates disease gene panels and facilitates sophisticated search. March 2025. doi: 10.1101/2025.03.20.25324319. URL http://medrxiv.org/lookup/doi/10.1101/2025.03.20.25324319.

[13] Antonio Rueda Martin, Eleanor Williams, Rebecca E. Foulger, Sarah Leigh, Louise C. Daugherty, Olivia Niblock, Ivone U. S. Leong, Katherine R. Smith, Oleg Gerasimenko, Eik Haraldsdottir, Ellen Thomas, Richard H. Scott, Emma Baple, Arianna Tucci, Helen Brittain, Anna De Burca, Kristina Ibañez, Dalia Kasperaviciute, Damian Smedley, Mark Caulfield, Augusto Rendon, and Ellen M. McDonagh. PanelApp crowdsources expert knowledge to establish consensus diagnostic gene panels. *Nature Genetics*, 51(11):1560–1565, November 2019. ISSN 1061-4036, 1546-1718. doi: 10.1038/s41588-019-0528-2. URL https://www.nature.com/articles/s41588-019-0528-2.

[14] M. Cecilia Poli, Ivona Aksentijevich, Ahmed Aziz Bousfiha, Charlotte Cunningham-Rundles, Sophie Hambleton, Christoph Klein, Tomohiro Morio, Capucine Picard, Anne Puel, Nima Rezaei, Mikko R.J. Seppänen, Raz Somech, Helen C. Su, Kathleen E. Sullivan, Troy R. Torgerson, Isabelle Meyts, and Stuart G. Tangye. Human inborn errors of immunity: 2024 update on the classification from the International Union of Immunological Societies Expert Committee. *Journal of Human Immunity*, 1(1):e20250003, May 2025. ISSN 3065-8993. doi: 10.70962/jhi.20250003. URL https://rupress.org/jhi/article/1/1/e20250003/277390/Human-inborn-errors-of-immunity-2024-update-on-the.

[15] Ahmed Aziz Bousfiha, Leïla Jeddane, Abderrahmane Moundir, M. Cecilia Poli, Ivona Aksentijevich, Charlotte Cunningham-Rundles, Sophie Hambleton, Christoph Klein, Tomohiro Morio, Capucine Picard, Anne Puel, Nima Rezaei, Mikko R.J. Seppänen, Raz Somech, Helen C. Su, Kathleen E. Sullivan, Troy R. Torgerson, Stuart G. Tangye, and Isabelle Meyts. The 2024 update of IUIS phenotypic classification of human inborn errors of immunity. *Journal of Human Immunity*, 1(1):e20250002, May 2025. ISSN 3065-8993. doi: 10.70962/jhi.20250002. URL https://rupress.org/jhi/article/1/1/e20250002/277374/The-2024-update-of-IUIS-phenotypic-classification.

[16] Xiaoming Liu, Chang Li, Chengcheng Mou, Yibo Dong, and Yicheng Tu. dbNSFP v4: a comprehensive database of transcript-specific functional predictions and annotations for human nonsynonymous and splice-site SNVs. *Genome Medicine*, 12(1):103, December 2020. ISSN 1756-994X. doi: 10.1186/s13073-020-00803-9. URL https://genomemedicine.biomedcentral.com/articles/10.1186/s13073-020-00803-9.

[17] Damian Szklarczyk, Katerina Nastou, Mikaela Koutrouli, Rebecca Kirsch, Farrokh Mehryary, Radja Hachilif, Dewei Hu, Matteo E Peluso, Qingyao Huang, Tao Fang, et al. The string database in 2025: protein networks with directionality of regulation. *Nucleic Acids Research*, 53(D1):D730–D737, 2025.

[18] Jun Cheng, Guido Novati, Joshua Pan, Clare Bycroft, Akvilė Žemgulytė, Taylor Applebaum, Alexander Pritzel, Lai Hong Wong, Michal Zielinski, Tobias Sargeant, Rosalia G. Schneider, Andrew W. Senior, John Jumper, Demis Hassabis, Pushmeet Kohli, and Žiga Avsec. Predictions for alphamissense, September 2023. URL https://doi.org/10.5281/zenodo.8208688.

[19] Paul Tuijnenburg, Hana Lango Allen, Siobhan O. Burns, Daniel Greene, Machiel H. Jansen, and Others. Loss-of-function nuclear factor B subunit 1 (NFKB1) variants are the most common monogenic cause of common variable immunodeficiency in Europeans. *Journal of Allergy and Clinical Immunology*, 142(4):1285–1296, October 2018. ISSN 00916749. doi: 10.1016/j.jaci.2018.01.039. URL https://linkinghub.elsevier.com/retrieve/pii/S0091674918302860.

[20] WHO Scientific Group et al. Primary immunodeficiency diseases: report of a who scientific group. *Clin. Exp. Immunol.*, 109(1):1–28, 1997.

[21] Charlotte Cunningham-Rundles and Carol Bodian. Common variable immunodeficiency: clinical and immunological features of 248 patients. *Clinical immunology*, 92(1):34–48, 1999.

[22] Eric Oksenhendler, Laurence Gérard, Claire Fieschi, Marion Malphettes, Gael Mouillot, Roland Jaussaud, Jean-François Viallard, Martine Gardembas, Lionel Galicier, Nicolas Schleinitz, et al. Infections in 252 patients with common variable immunodeficiency. *Clinical Infectious Diseases*, 46(10):1547–1554, 2008.

[23] Y Naito, F Adams, S Charman, J Duckers, G Davies, and S Clarke. Uk cystic fibrosis registry 2023 annual data report. *London: Cystric Fibrosis Trust*, 2023.

[24] Carlo Castellani, CFTR2 team, et al. Cftr2: how will it help care? *Paediatric respiratory reviews*, 14:2–5, 2013.

[25] Hartmut Grasemann and Felix Ratjen. Cystic fibrosis. *New England Journal of Medicine*, 389(18):1693–1707, 2023. doi: 10.1056/NEJMra2216474. URL https://www.nejm.org/doi/full/10.1056/NEJMra2216474.

[26] Kyoko Watanabe, Erdogan Taskesen, Arjen Van Bochoven, and Danielle Posthuma. Functional mapping and annotation of genetic associations with FUMA. *Nature Communications*, 8(1):1826, November 2017. ISSN 2041-1723. doi: 10.1038/s41467-017-01261-5. URL https://www.nature.com/articles/s41467-017-01261-5.

[27] Arthur Liberzon, Aravind Subramanian, Reid Pinchback, Helga Thorvaldsdóttir, Pablo Tamayo, and Jill P. Mesirov. Molecular signatures database (MSigDB) 3.0. *Bioinformatics*, 27(12):1739–1740, June 2011. ISSN 1367-4811, 1367-4803. doi: 10.1093/bioinformatics/btr260. URL https://academic.oup.com/bioinformatics/article/27/12/1739/257711.

[28] Dylan Lawless. Variant risk estimate probabilities for iei genes. March 2025. doi: 10.5281/zenodo.15111584. URL https://doi.org/10.5281/zenodo.15111584.

[29] Eric Vallabh Minikel, Sonia M. Vallabh, Monkol Lek, Karol Estrada, Kaitlin E. Samocha, J. Fah Sathirapongsasuti, Cory Y. McLean, Joyce Y. Tung, Linda P. C. Yu, Pierluigi Gambetti, Janis Blevins, Shulin Zhang, Yvonne Cohen, Wei Chen, Masahito Yamada, Tsuyoshi Hamaguchi, Nobuo Sanjo, Hidehiro Mizusawa, Yosikazu Nakamura, Tetsuyuki Kitamoto, Steven J. Collins, Alison Boyd, Robert G. Will, Richard Knight, Claudia Ponto, Inga Zerr, Theo F. J. Kraus, Sabina Eigenbrod, Armin Giese, Miguel Calero, Jesús De Pedro-Cuesta, Stéphane Haïk, Jean-Louis Laplanche, Elodie Bouaziz-Amar, Jean-Philippe Brandel, Sabina Capellari, Piero Parchi, Anna Poleggi, Anna Ladogana, Anne H. O'Donnell-Luria, Konrad J. Karczewski, Jamie L. Marshall, Michael Boehnke, Markku Laakso, Karen L. Mohlke, Anna Kähler, Kimberly Chambert, Steven McCarroll, Patrick F. Sullivan, Christina M. Hultman, Shaun M. Purcell, Pamela Sklar, Sven J. Van Der Lee, Annemieke Rozemuller, Casper Jansen, Albert Hofman, Robert Kraaij, Jeroen G. J. Van Rooij, M. Arfan Ikram, André G. Uitterlinden, Cornelia M. Van Duijn, Exome Aggregation Consortium (ExAC), Mark J. Daly, and Daniel G. MacArthur. Quantifying prion disease penetrance using large population control cohorts. *Science Translational Medicine*, 8(322), January 2016. ISSN 1946-6234, 1946-6242. doi: 10.1126/scitranslmed.aad5169. URL https://www.science.org/doi/10.1126/scitranslmed.aad5169.

[30] Nicola Whiffin, Eric Minikel, Roddy Walsh, Anne H O'Donnell-Luria, Konrad Karczewski, Alexander Y Ing, Paul J R Barton, Birgit Funke, Stuart A Cook, Daniel MacArthur, and James S Ware. Using high-resolution variant frequencies to empower clinical genome interpretation. *Genetics in Medicine*, 19(10):1151–1158, October 2017. ISSN 10983600. doi: 10.1038/gim.2017.26. URL https://linkinghub.elsevier.com/retrieve/pii/S1098360021013678.

[31] Bradley Efron and Carl Morris. Stein's Estimation Rule and Its Competitors–An Empirical Bayes Approach. *Journal of the American Statistical Association*, 68(341):117, March 1973. ISSN 01621459. doi: 10.2307/2284155. URL https://www.jstor.org/stable/2284155?origin=crossref.

[32] Yaowu Liu, Sixing Chen, Zilin Li, Alanna C Morrison, Eric Boerwinkle, and Xihong Lin. Acat: a fast and powerful p value combination method for rare-variant analysis in sequencing studies. *The American Journal of Human Genetics*, 104(3):410–421, 2019.

[33] Xihao Li, Zilin Li, Hufeng Zhou, Sheila M Gaynor, Yaowu Liu, Han Chen, Ryan Sun, Rounak Dey, Donna K Arnett, Stella Aslibekyan, et al. Dynamic incorporation of multiple in silico functional annotations empowers rare variant association analysis of large whole-genome sequencing studies at scale. *Nature genetics*, 52 (9):969–983, 2020.

[34] Michael C Wu, Seunggeun Lee, Tianxi Cai, Yun Li, Michael Boehnke, and Xihong Lin. Rare-variant association testing for sequencing data with the sequence kernel association test. *The American Journal of Human Genetics*, 89(1):82–93, 2011.

[35] Seunggeun Lee, Mary J Emond, Michael J Bamshad, Kathleen C Barnes, Mark J Rieder, Deborah A Nickerson, David C Christiani, Mark M Wurfel, and Xihong Lin. Optimal unified approach for rare-variant association testing with application to small-sample case-control whole-exome sequencing studies. *The American Journal of Human Genetics*, 91(2):224–237, 2012.

[36] Augustine Kong, Gudmar Thorleifsson, Michael L Frigge, Bjarni J Vilhjalmsson, Alexander I Young, Thorgeir E Thorgeirsson, Stefania Benonisdottir, Asmundur Oddsson, Bjarni V Halldorsson, Gisli Masson, et al. The nature of nurture: Effects of parental genotypes. *Science*, 359(6374):424–428, 2018.

[37] Laurence J Howe, Michel G Nivard, Tim T Morris, Ailin F Hansen, Humaira Rasheed, Yoonsu Cho, Geetha Chittoor, Penelope A Lind, Teemu Palviainen, Matthijs D van der Zee, et al. Within-sibship gwas improve estimates of direct genetic effects. *BioRxiv*, pages 2021–03, 2021.

[38] Sue Richards, Nazneen Aziz, Sherri Bale, David Bick, Soma Das, Julie Gastier-Foster, Wayne W Grody, Madhuri Hegde, Elaine Lyon, Elaine Spector, et al. Standards and guidelines for the interpretation of sequence variants: a joint consensus recommendation of the american college of medical genetics and genomics and the association for molecular pathology. *Genetics in medicine*, 17 (5):405–423, 2015.

[39] Sean V Tavtigian, Steven M Harrison, Kenneth M Boucher, and Leslie G Biesecker. Fitting a naturally scaled point system to the acmg/amp variant classification guidelines. *Human mutation*, 41(10):1734–1737, 2020.

[40] Quan Li and Kai Wang. Intervar: clinical interpretation of genetic variants by the 2015 acmg-amp guidelines. *The American Journal of Human Genetics*, 100 (2):267–280, 2017.

[41] Brent S Pedersen, Joe M Brown, Harriet Dashnow, Amelia D Wallace, Matt Velinder, Martin Tristani-Firouzi, Joshua D Schiffman, Tatiana Tvrdik, Rong Mao, D Hunter Best, et al. Effective variant filtering and expected candidate variant yield in studies of rare human disease. *NPJ Genomic Medicine*, 6(1):1–8, 2021.

[42] Carl A Anderson, Fredrik H Pettersson, Geraldine M Clarke, Lon R Cardon, Andrew P Morris, and Krina T Zondervan. Data quality control in genetic case-control association studies. *Nature protocols*, 5(9):1564–1573, 2010. URL https://doi.org/10.1038/nprot.2010.116.

[43] David T Miller, Kristy Lee, Noura S Abul-Husn, Laura M Amendola, Kyle Brothers, Wendy K Chung, Michael H Gollob, Adam S Gordon, Steven M Harrison, Ray E Hershberger, et al. Acmg sf v3. 2 list for reporting of secondary findings in clinical exome and genome sequencing: a policy statement of the american college of medical genetics and genomics (acmg). *Genetics in Medicine*, 25(8): 100866, 2023.

6 Supplemental

Supplemental data are presented under the same headings that correspond to their relevant main text sections.

6.1 Variant class occurrence probability

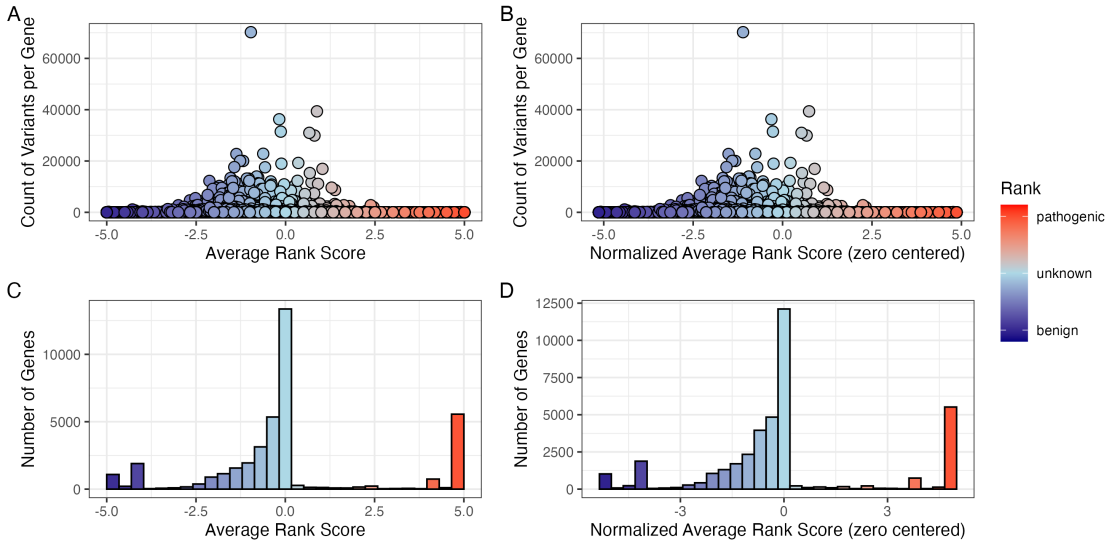

Figure S1: **Global distribution of ClinVar clinical-significance classification scoring.** (A) Number of variants per gene containing the assigned score for each ClinVar classification term (−5 to +5). (B) The same data after normalisation by zero centring the average rank score. (C) The tally of genes for their average rank and (D) after normalisation. No normalisation was required for the scoring system as shown by comparison of A-C and B-D.

6.2 Integrating observed true positives and unobserved false negatives into a single, actionable conclusion

Table S1: Result of clinical genetics diagnosis scenario 1 including metadata. The most strongly supported observed variant was `p.Ser237Ter` (posterior: 0.594). The strongest unsequenced variant was `p.Thr567Ile` (posterior: 0). The total probability of a causal diagnosis given the available evidence was 1 (95% CI: 1–1).

Variant	Flag	Class	Evidence Score	Occurrence Prob	Adj Occ Prob	Alpha	Beta	Lower	Median	Upper	Posterior Share	Prob Causal
p.Ser237Ter	present	causal	5	0.000	0	6	371	0.004	0.142	0.803	0.594	0.594
p.Thr567Ile	missing	other	-5	0.002	0	1	363	NA	NA	NA	0.000	0.000
p.Arg231His	present	other	0	0.000	0	1	361	0.004	0.142	0.803	0.000	0.000
p.Gly650Arg	present	other	0	0.000	0	1	379	0.004	0.142	0.803	0.000	0.000
p.Val236Ile	missing	other	0	0.000	0	1	351	NA	NA	NA	0.000	0.000
Total	NA	NA	NA	NA	NA	NA	NA	1.000	1.000	1.000	NA	1.000

Table S2: Result of clinical genetics diagnosis scenario 2 including metadata. The most strongly supported observed variant was `p.Ser237Ter` (posterior: 0.381). The strongest unsequenced variant was `c.159+1G>A` (posterior: 0.353). The total probability of a causal diagnosis given the available evidence was 0.52 (95% CI: 0.248–0.787).

Variant	Flag	Class	Evidence Score	Occurrence Prob	Adj Occ Prob	Alpha	Beta	Lower	Median	Upper	Posterior Share	Prob Causal
p.Ser237Ter	present	causal	5.0	0.000	0	6.0	371	0.003	0.096	0.557	0.381	0.381
c.159+1G>A	missing	causal	4.5	0.000	0	5.5	367	NA	NA	NA	0.353	0.353
p.Thr567Ile	missing	other	-5.0	0.002	0	1.0	365	NA	NA	NA	0.000	0.000
p.Arg231His	present	other	0.0	0.000	0	1.0	359	0.003	0.096	0.557	0.000	0.000
p.Gly650Arg	present	other	0.0	0.000	0	1.0	349	0.003	0.096	0.557	0.000	0.000
p.Val236Ile	missing	other	0.0	0.000	0	1.0	363	NA	NA	NA	0.000	0.000
Total	NA	NA	NA	NA	NA	NA	NA	0.248	0.520	0.787	NA	0.520

Table S3: Result of clinical genetics diagnosis scenario 3 including metadata. No observed variants were detected in this scenario. The strongest unsequenced variant was `p.Cys243Arg` (posterior: 0.366). The total probability of a causal diagnosis given the available evidence was 0 (95% CI: 0–0).

Variant	Flag	Class	Evidence Score	Occurrence Prob	Adj Occ Prob	Alpha	Beta	Lower	Median	Upper	Posterior Share	Prob Causal
p.Cys243Arg	missing	causal	5.0	0.000	0.000	6	341	NA	NA	NA	0.366	0.366
p.Tyr246Ter	missing	causal	4.0	0.000	0.000	5	369	NA	NA	NA	0.284	0.284
p.Lys304Glu	missing	other	-5.0	0.000	0.000	1	353	NA	NA	NA	0.000	0.000
p.Ile207Leu	missing	other	-4.5	0.000	0.000	1	359	NA	NA	NA	0.000	0.000
p.His646Pro	missing	other	0.0	0.002	0.001	1	377	NA	NA	NA	0.000	0.000
p.Arg280Trp	missing	other	-4.0	0.000	0.000	1	357	NA	NA	NA	0.000	0.000
p.Thr635Ile	missing	other	0.0	0.000	0.000	1	349	NA	NA	NA	0.000	0.000
p.Arg162Trp	missing	other	0.0	0.000	0.000	1	369	NA	NA	NA	0.000	0.000
Total	NA	NA	NA	NA	NA	NA	NA	0	0	0	NA	0.000

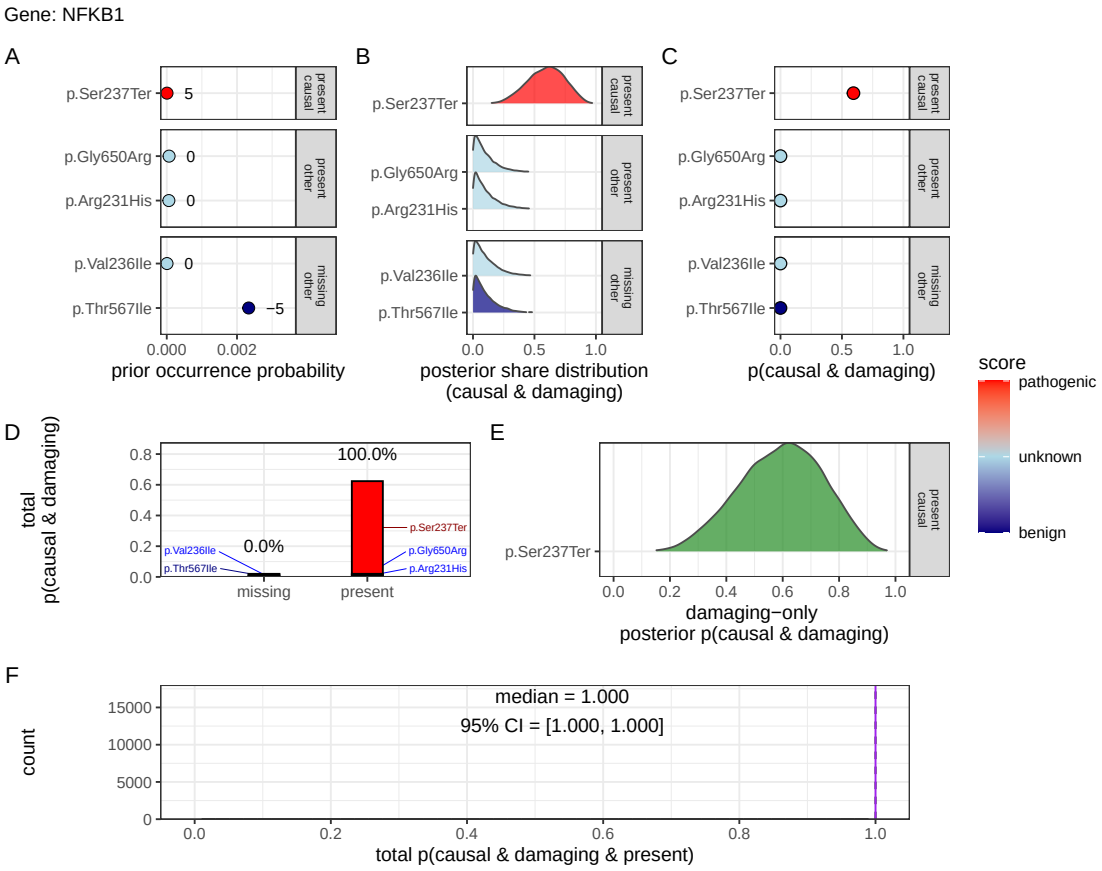

Figure S2: **Quantification of present (TP) and no missing (FN) causal genetic variants for disease in *NFKB1* (scenario 1)**. Only one known pathogenic variant, `p.Ser237Ter`, was observed and all previously reported pathogenic positions were successfully sequenced and confirmed as reference (true negatives). Panels (A–F) follow the same structure as scenario 2 described in **Figure 2**, culminating in a gene-level posterior probability of 1 (95 % CrI: 0.99–1.00), with full support assigned to the observed allele given the available evidence. Pathogenicity scores (-5 to +5) are annotated.

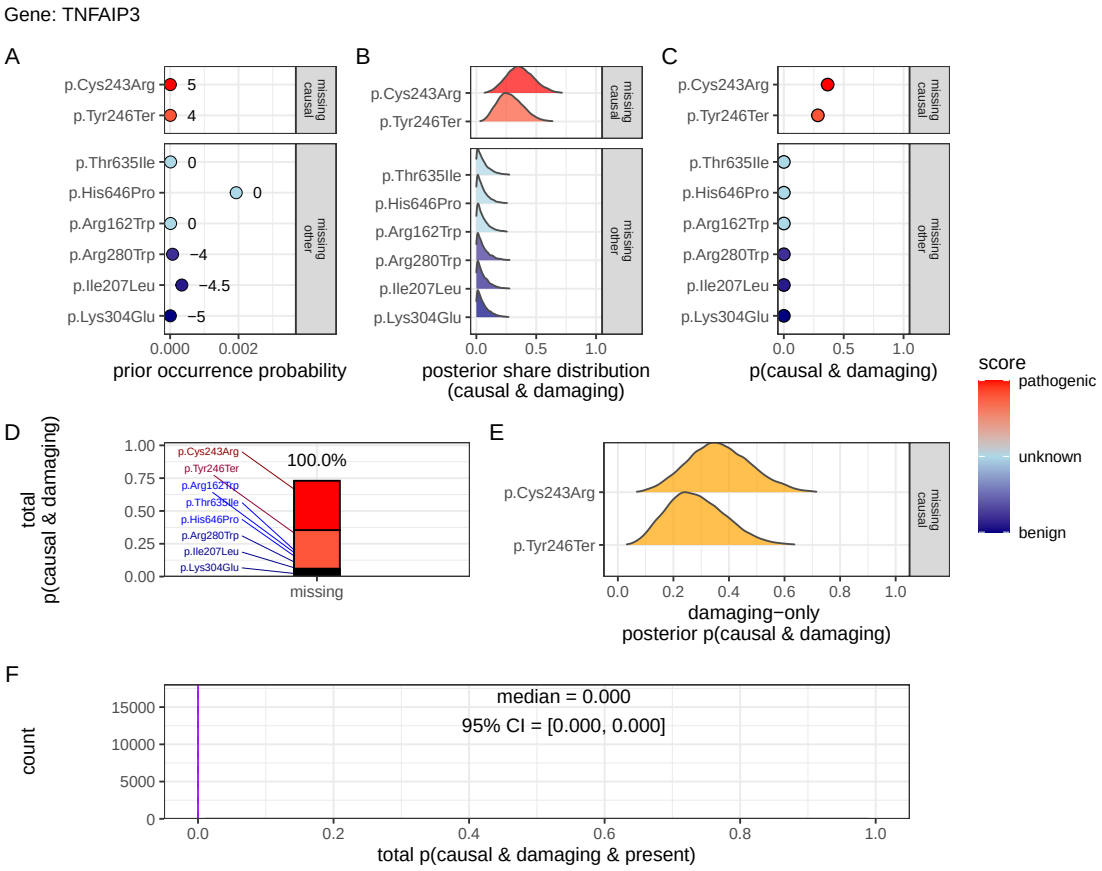

Figure S3: **Quantification of no present (TP) in *NFKB1* and only missing (FN) causal genetic variants for disease in *TNFAIP3* (scenario 3)**. No known causal variants were observed in *NFKB1*, but one representative unsequenced allele was selected from each distinct ClinVar classification and treated as a potential false negative. Panels (A–F) follow the same structure as scenario 2 described in **Figure 2**. The posterior reflects uncertainty across multiple plausible but unobserved variants, resulting in low CrI (0-0) and 100% missing overall attribution in contrast to scenarios where known pathogenic variants were observed. For this patient, we have no evidence of a causal variant since the only top candidates are not yet accounted for. Pathogenicity scores (-5 to +5) are annotated in (A).

6.3 Validation studies

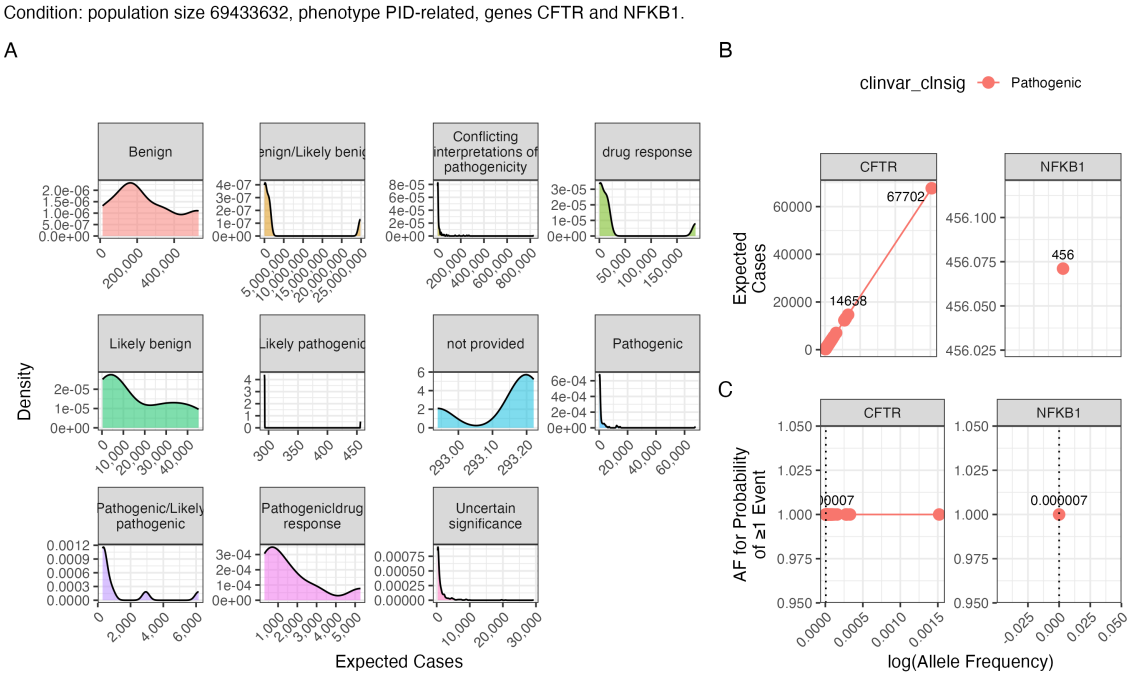

Figure S4: **Interpretation of probability of observing a variant classification.** The result from the chosen validation genes *CFTR* and *NFKB1* are shown. Case counts are dependant on the population size and phenotype. (A) The density plots of expected observations by ClinVar clinical significance. We then highlight the values for pathogenic variants specifically showing; (B) the allele frequency versus expected cases in this population size and (C) the probability of observing at least one event in this population size.

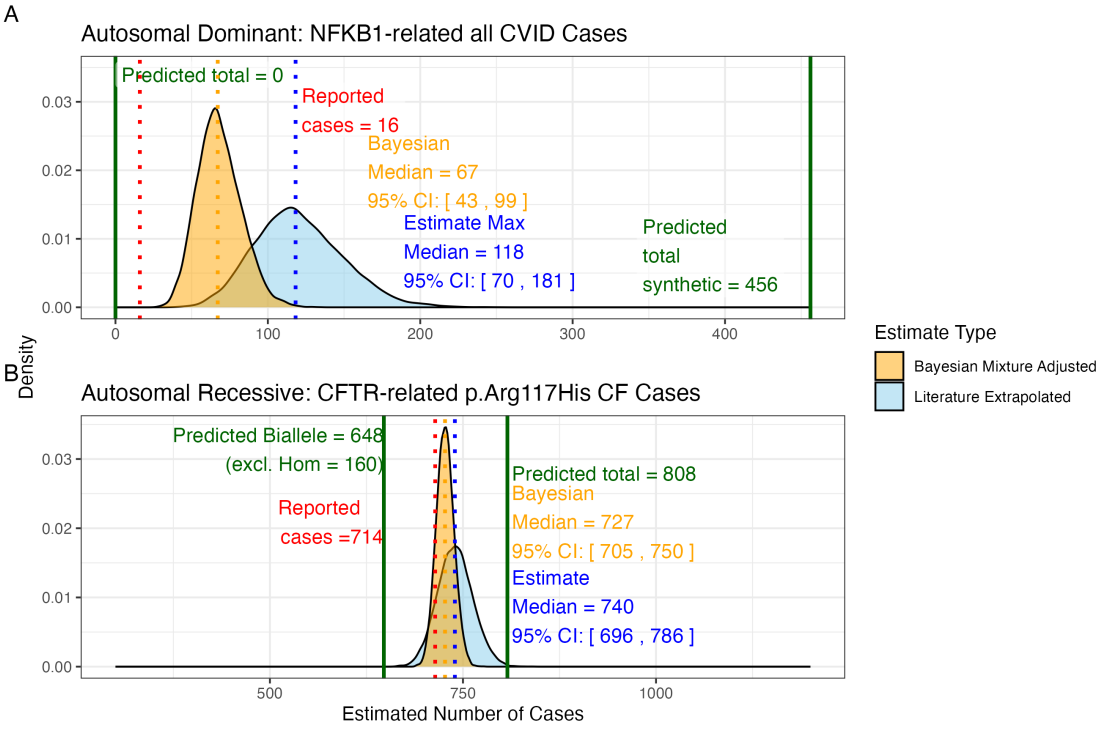

Figure S5: **Prior probabilities compared to validation disease cohort metrics.** (A) Density distributions for the number of *NFKB1*-related CVID cases in the UK. Our model (green) predicted 456 cases, which falls between the observed cohort count (red) of 390 and the upper extrapolated values. The blue curve represents maximum count of 1280, and the orange curve shows the Bayesian-adjusted mixture estimate of 835. (B) Density distributions for *CFTR*-related `p.Arg117His` CF cases. Our model (green) predicted 648 biallelic cases and 808 total cases. The nationally reported case count (red) was 714. The blue curve represents maximum extrapolated count of 740, and the orange curve shows the Bayesian-adjusted mixture estimate of 727. We observed close agreement among the reported disease cases and our integrated probability estimation framework.

6.3.1 Interpretation of ClinVar variant observations

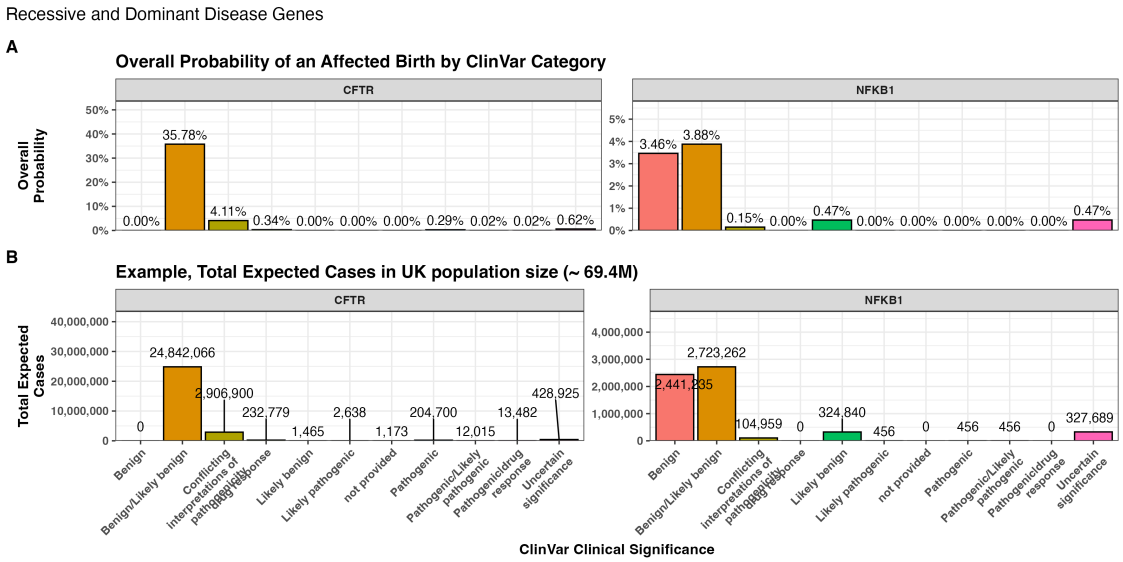

Figure S6: **Combined bar charts summarising the genome-wide analysis of ClinVar clinical significance for the PID gene panel**. Panel (A) shows the overall probability of an affected birth by variant classification, and (B) displays the total expected number of cases per classification, both stratified by gene. These integrated results illustrate the variability in variant observations across genes and underpin our validation of the probability estimation framework.

6.3.2 Validation of SCID-specific disease occurrence

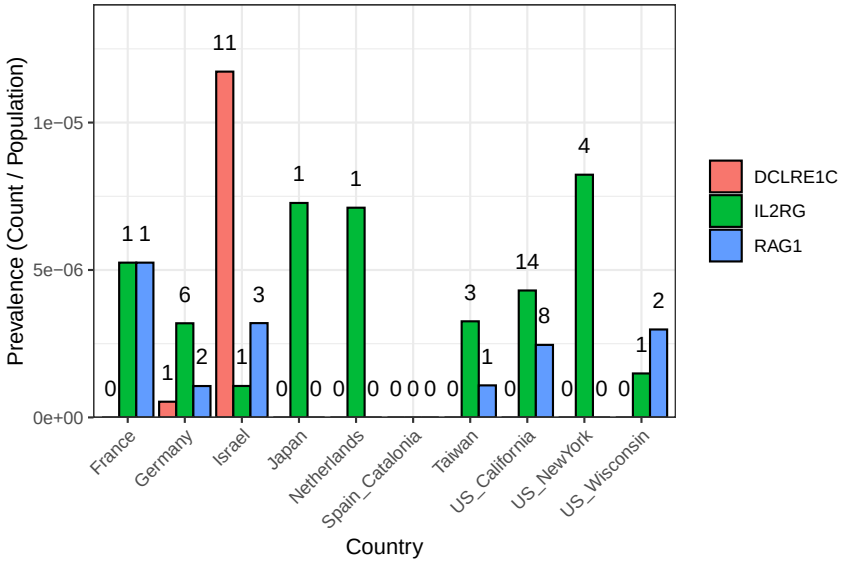

Figure S7: **SCID-specific gene comparison across regions.** The bar plot shows the prevalence of SCID-related cases (count divided by population) for each gene and country (or region), with numbers printed above the bars representing the actual counts in the original cohort (ranging from 0 to 11 per region and gene).

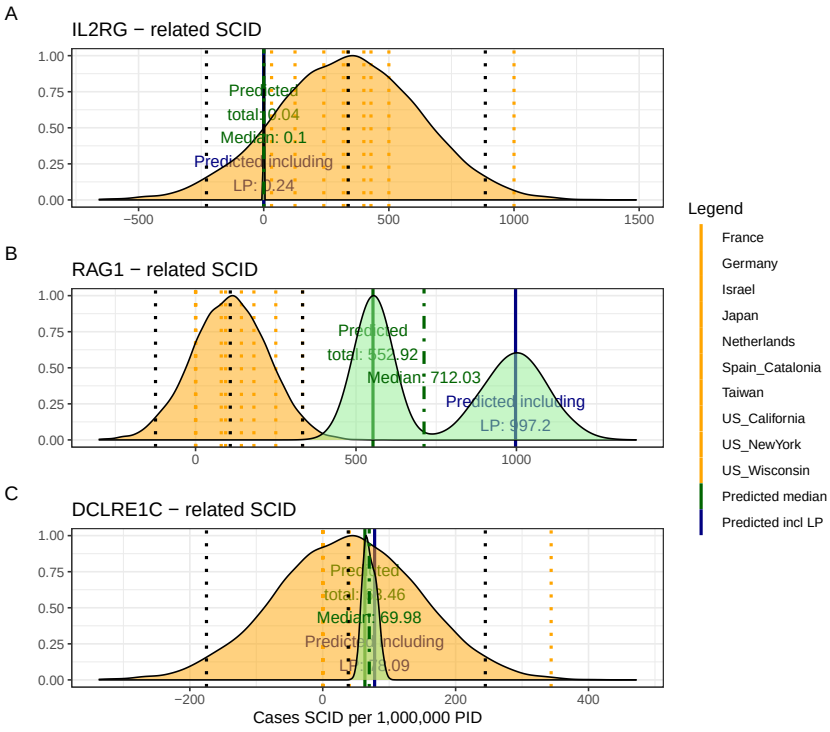

Figure S8: **Combined SCID-specific Predictions and Observed Rates per 1,000,000 PID.** The figure presents density distributions for the predicted SCID case counts (per 1,000,000 PID) for three genes: *IL2RG*, *RAG1*, and *DCLRE1C*. Country-specific rates (displayed as dotted vertical lines) are overlaid with the overall predicted distributions for pathogenic and likely pathogenic variants (solid lines with annotated medians). For *IL2RG*, the low predicted value is consistent with the high deleteriousness of loss-of-function variants in this X-linked gene, while *RAG1* exhibits considerably higher predicted counts, reflecting its lower penetrance in an autosomal recessive context.

6.4 Genetic constraint in high-impact protein networks

6.4.1 Score-positive-total within IEI PPI network

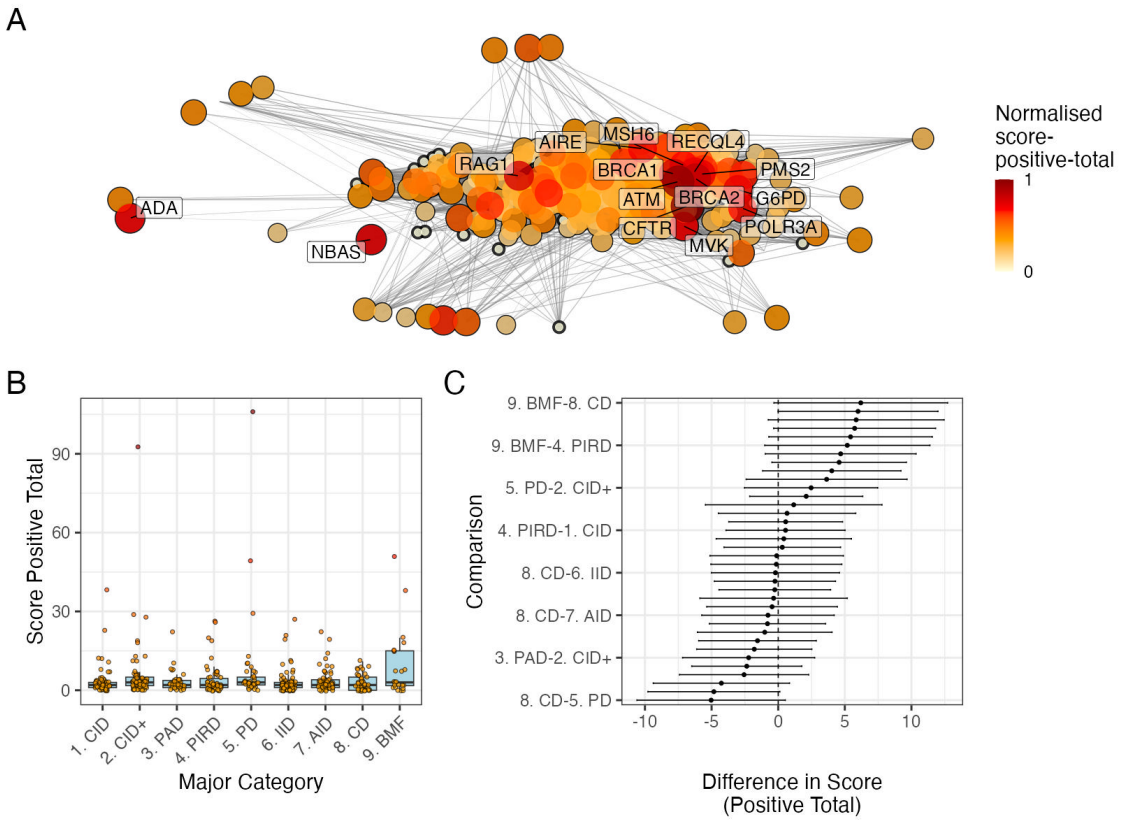

Figure S9: **PPI network and score-positive-total ClinVar significance variants**. (A) PPI network of disease-associated genes. Node size and colour represent the log-transformed score-positive-total, the top 15 genes/proteins with the highest probability of being observed in disease are labelled. (B) Distribution of score-positive-total across the major IEI disease categories. (C) Tukey HSD comparisons of mean differences in score-positive-total among all pairwise disease categories. Every 5th label is shown on y-axis.

6.4.2 Hierarchical Clustering of Enrichment Scores for Major Disease Categories

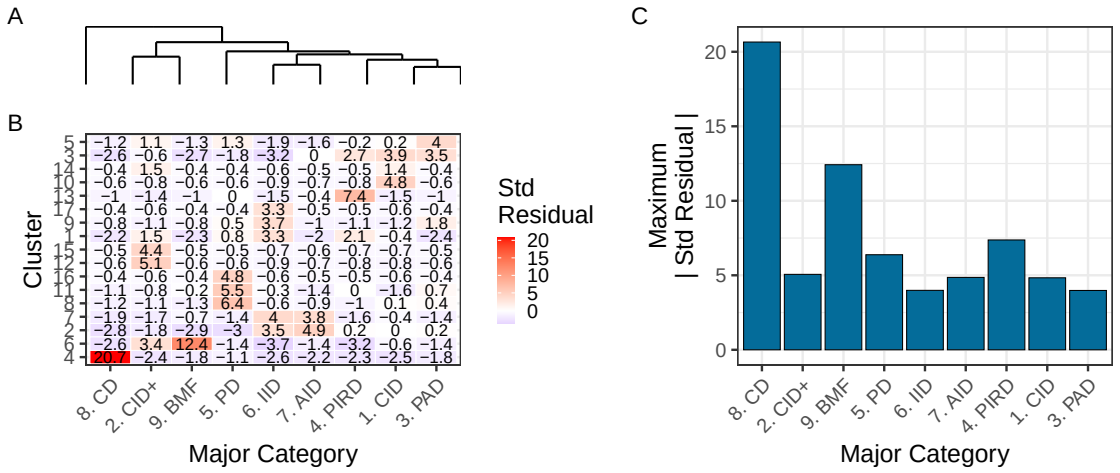

Figure S10: **Hierarchical clustering of enrichment scores.** The heatmap displays standardised residuals for major disease categories (x-axis) across network clusters (y-axis). A dendrogram groups similar disease categories, and the bar plot shows the maximum absolute residual per category. (8) CD and (9)BMF show the highest vales, indicating significant enrichment or depletion (residuals $> |2|$). Definitions in **Box 2.1**.

6.4.3 PPI connectivity, LOEUF constraint and enriched network cluster analysis

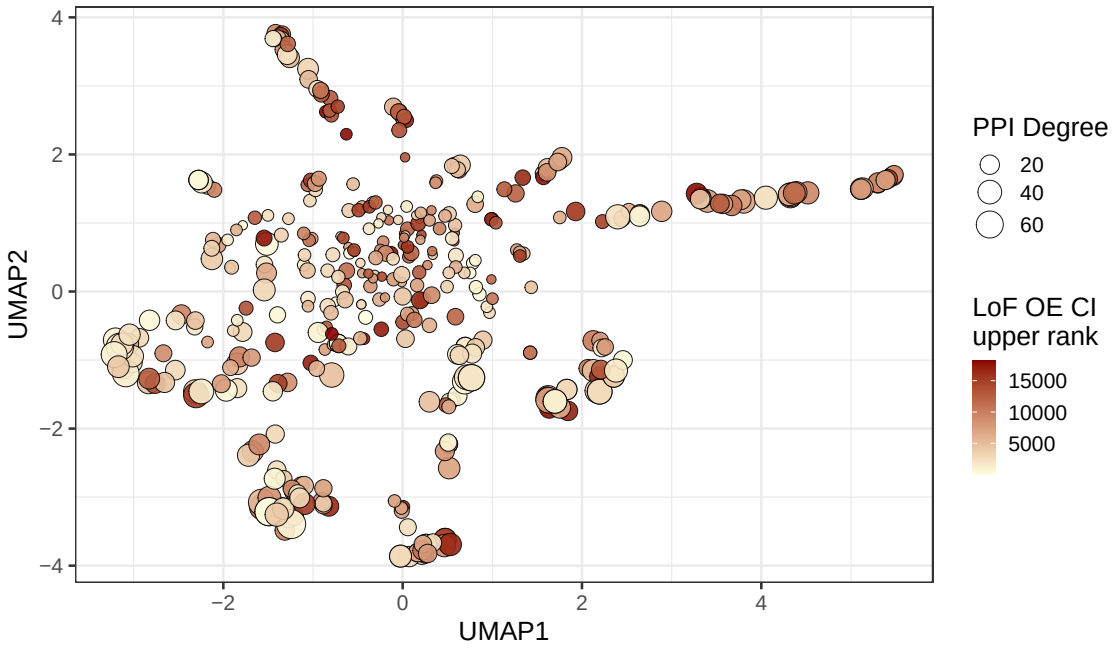

Figure S11: **Analysis of PPI degree versus LOEUF upper rank with UMAP embedding of the PPI network.** The relationship between PPI degree (size) and LOEUF upper rank (color) across gene clusters. No clear patterns are evident.

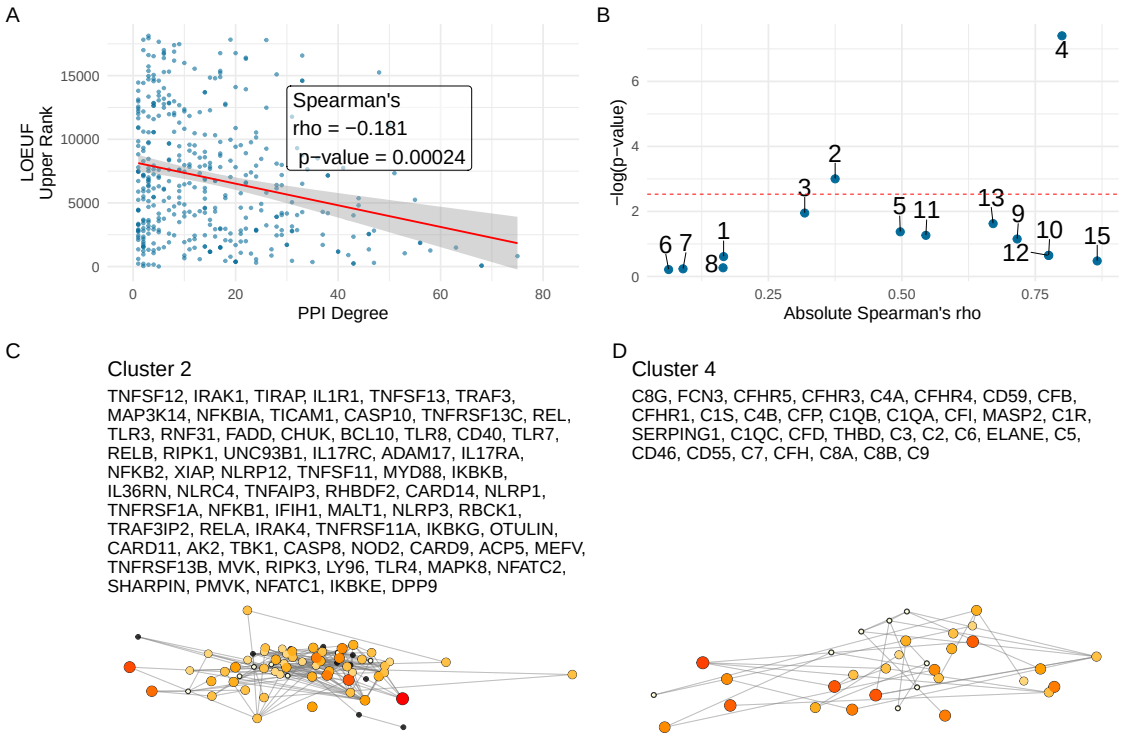

Figure S12: **Correlation between PPI degree and LOEUF upper rank. (A)** Ananlysis across all genes revealed a weak, significant negative correlation between PPI degree and LOEUF upper rank. **(B)** The cluster-wise analysis showed that clusters 2 and 4 exhibited moderate to strong correlations, while other clusters display weak or non-significant relationships. **(C) and (D)** Shows the new network plots for the significantly enriched clusters based on gnomAD constraint metrics.

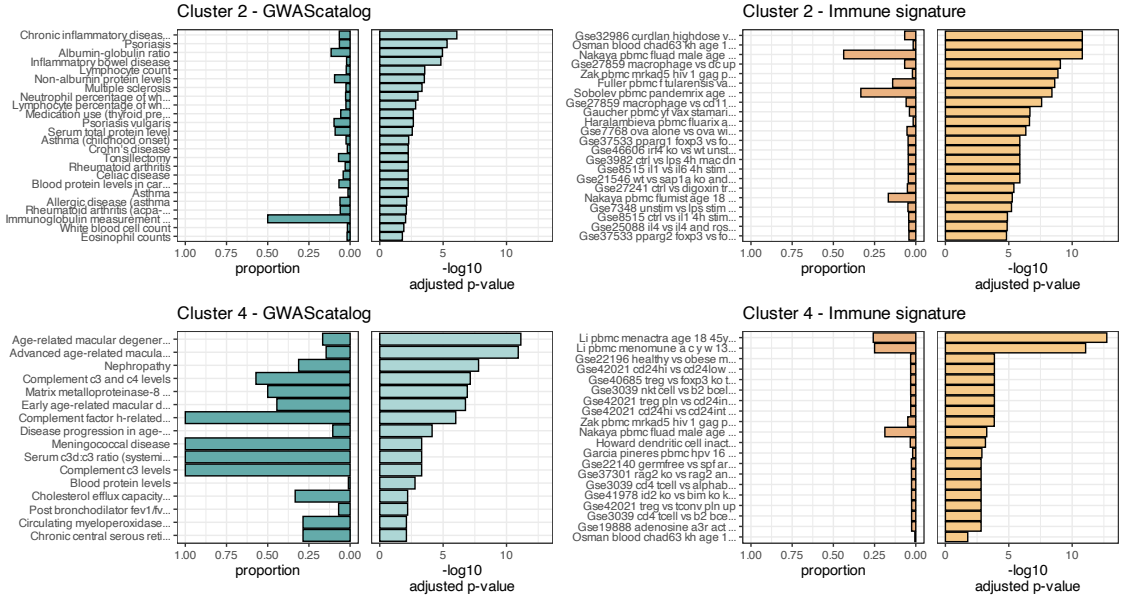

Figure S13: **Composite Enrichment Profiles for IEI Gene Sets.** We selected the top two enriched clusters (as per **Figure S12**) and performed functional enrichment analysis derived from known disease associations. For each gene set, the left panel displays the proportion of input genes overlapping with a curated gene set, and the right panel shows the $-\log_{10}$ adjusted p-value from hypergeometric testing. These profiles, stratified by cluster (Cluster 2 and Cluster 4) and by gene set category (GWAScatalog and Immunologic Signatures), highlight distinct enrichment patterns that reflect differential pathogenic variant loads in the IEI gene panels.

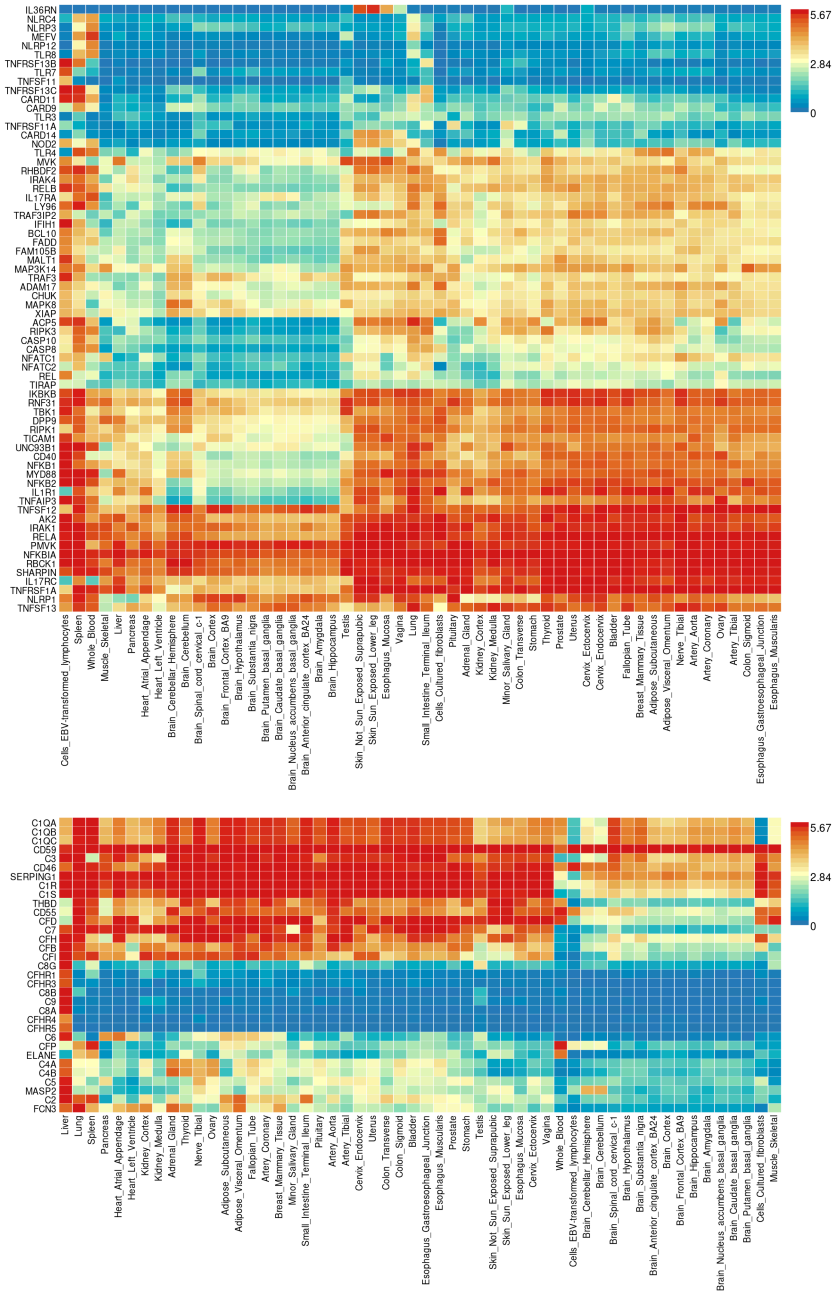

Figure S14: **Gene Expression Heatmaps for IEI Genes.** GTEx v8 data from 54 tissue types display the average expression per tissue label ($\log_2$ transformed) for the IEI gene panels. Top: Cluster 2; Bottom: Cluster 4.

6.5 Novel PID classifications derived from genetic PPI and clinical features

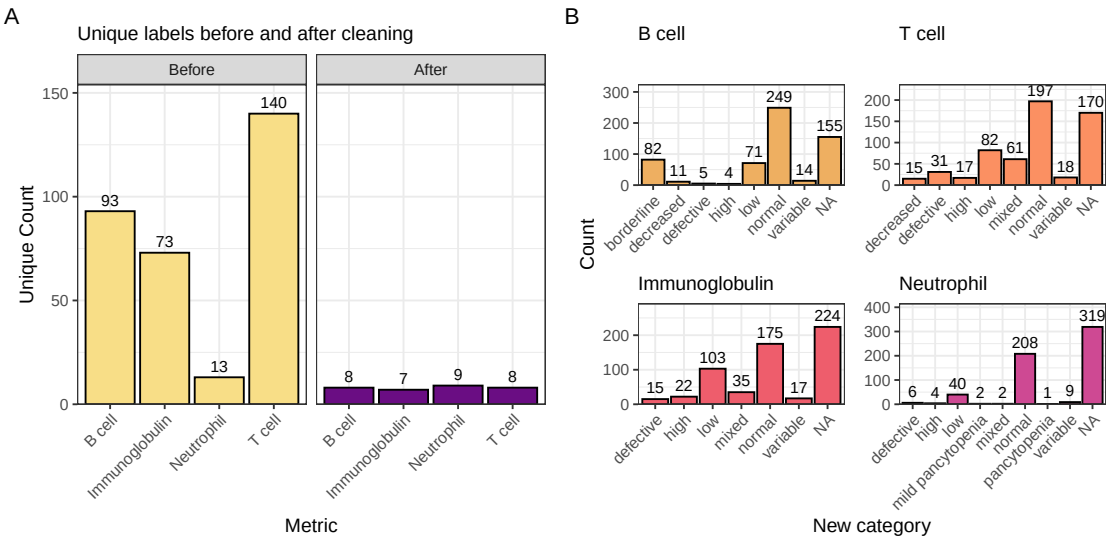

Figure S15: **Distribution of immunophenotypic features before and after recategorisation.** The original IUIS IEI descriptions contain information such as T cell-related "decreased CD8, normal or decreased CD4 cells" which we recategorise as "low". The bar plot shows the count of unique labels for each status (normal, not_normal) across the T cell, B cell, Ig, and Neutrophil features.

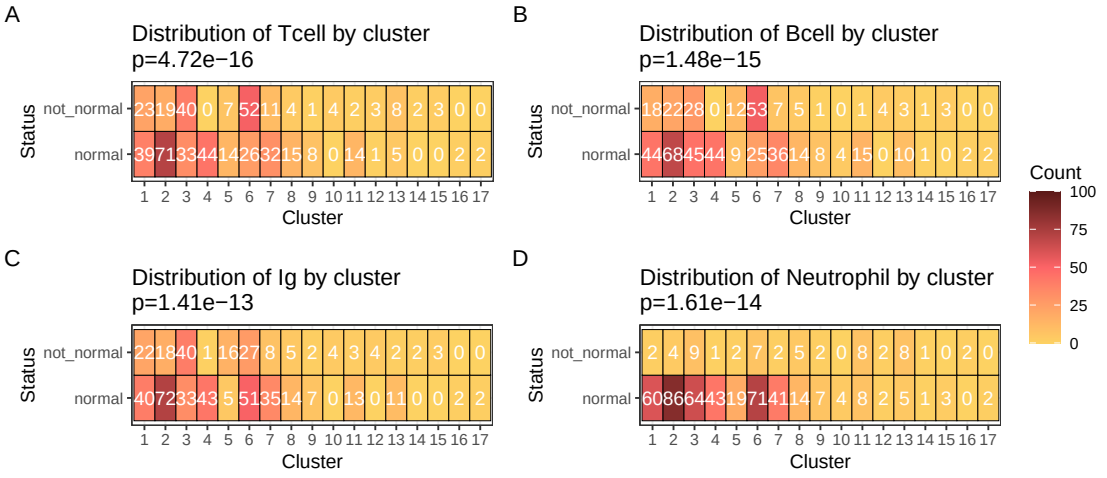

Figure S16: **Heatmaps of clinical feature distributions by PPI cluster.** The heatmaps display the count of observations for abnormality of each clinical feature (A) T cell, (B) B cell, (C) Immunoglobulin, (D) Neutrophil, in relation to the PPI clusters, with p-values from chi-square tests annotated in the titles.

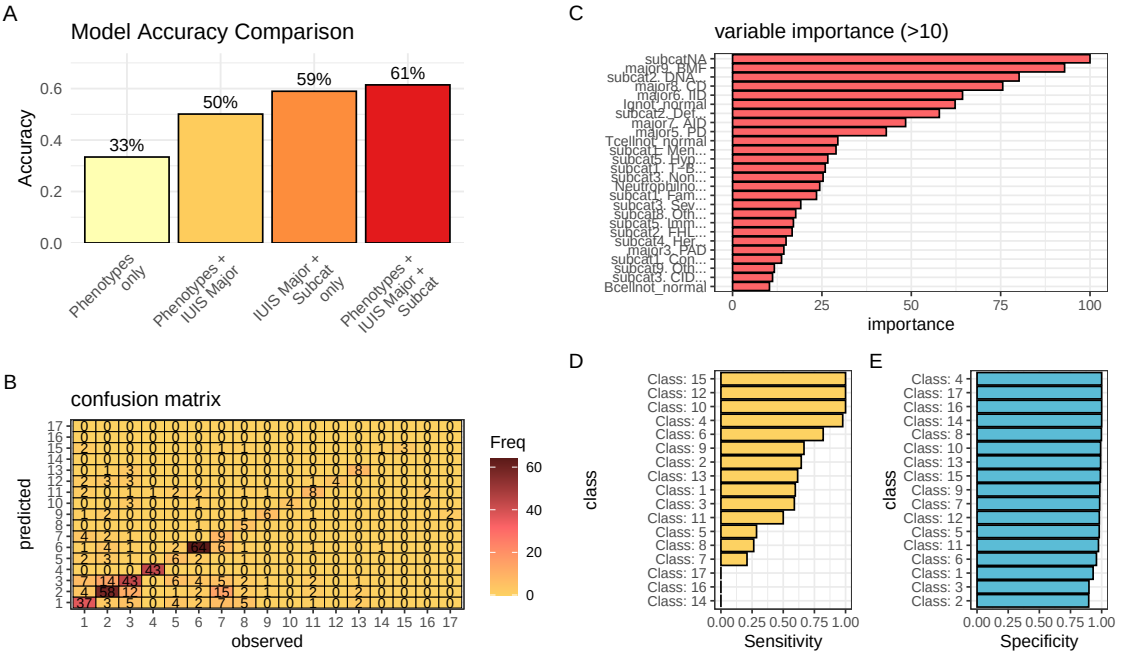

Figure S17: **Performance comparison of PID classifiers.** Classification predicting PPI cluster membership from IUIS major category, subcategory, and immunological features. (A) Overall accuracy for four rpart models used to predict PPI clustering. The combined model achieves 61.4 % accuracy, exceeding all simpler approaches. Nodes were split to minimize Gini impurity, pruned by cost-complexity (cp = 0.001), and validated via 5-fold cross-validation. (B-E) The summary statistics from the top model are detailed.

6.6 Probability of observing AlphaMissense pathogenicity

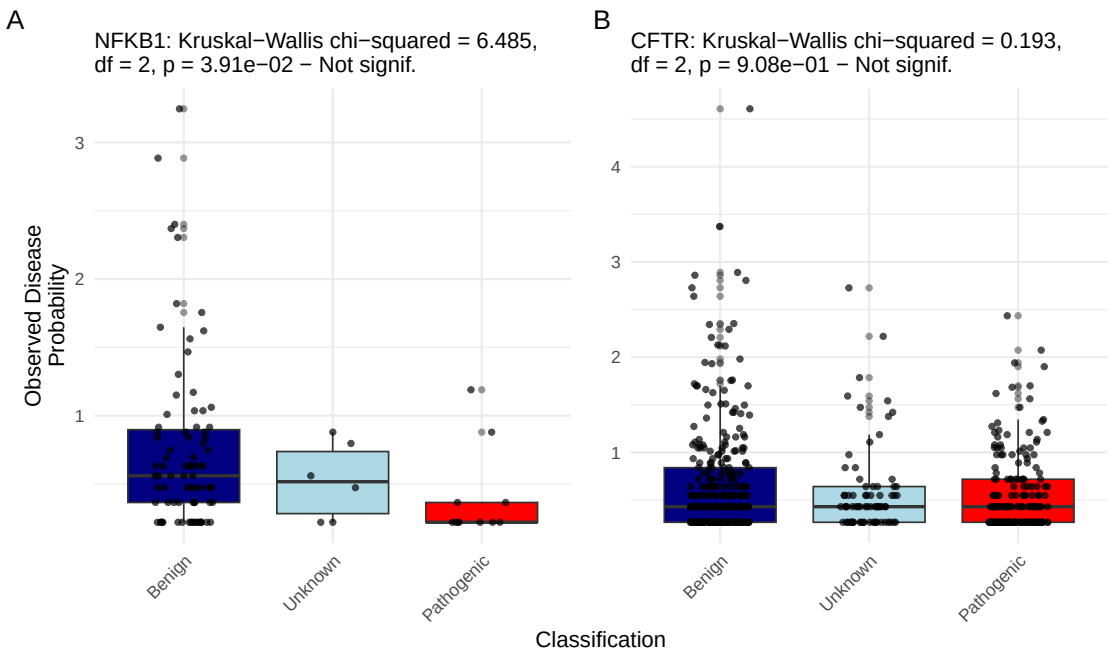

Figure S18: **Observed Disease Probability by Clinical Classification with AlphaMissense.** The figure displays the Kruskal-Wallis test results for NFKB1 and CFTR, showing no significant differences.